Journal of Computational Physics 440 (2021) 110403

Contents lists available at ScienceDirect

Journal of Computational Physics

www.elsevier.com/locate/jcp

Adjoint-based sensitivity analysis of periodic orbits by the Fourier–Galerkin method

J. Sierra [a,b], P. Jolivet [c], F. Giannetti [b,*], V. Citro [b]

[a] Institut de m'ecanique des fluides de Toulouse (IMFT), Toulouse 31400, France
[b] Dipartimento di Ingegneria (DIIN), Universitá degli Studi di Salerno, Fisciano 84084, Italy
[c] CNRS-IRIT, 2 rue Charles Camichel, 31071 Toulouse Cedex 7, France

ARTICLE INFO

Article history:
Available online 13 May 2021

Keywords:
Sensitivity
Fourier–Galerkin method
Floquet stability analysis
Unstable periodic orbits

ABSTRACT

Sensitivity of periodic solutions of time-dependent partial differential equations is commonly computed using time-consuming direct and adjoint time integrations. Particular attention must be provided to the periodicity condition in order to obtain accurate results. Furthermore, stabilization techniques are required if the orbit is unstable. The present article aims to propose an alternative methodology to evaluate the sensitivity of periodic flows via the Fourier–Galerkin method. Unstable periodic orbits are directly computed and continued without any stabilizing technique. The stability of the periodic state is determined via Hill's method: the frequency-domain counterpart of Floquet analysis. Sensitivity maps, used for open-loop control and physical instability identification, are directly evaluated using the adjoint of the projected operator. Furthermore, we propose an efficient and robust iterative algorithm for the resolution of underlying linear systems. First of all, the new approach is applied on the Feigenbaum route to chaos in the Lorenz system. Second, the transition to a three-dimensional state in the periodic vortex-shedding past a circular cylinder is investigated. Such a flow case allows the validation of the sensitivity approach by a systematic comparison with previous results presented in the literature. Finally, the transition to a quasi-periodic state past two side-by-side cylinders is considered. These last two cases also served to test the performance of the proposed iterative algorithm.

1. Introduction

Steady and periodic states of continuous and discrete dynamical systems are the two simplest cases of invariant sets which are of fundamental importance to characterize dynamics and to design efficient control strategies. Limit cycles may be found in almost every field of physics and applied mathematics. Some complex structures of the phase space, such as invariant tori or some strange attractors, may be preceded by a stable periodic solution. The continuation of these periodic solutions beyond their domain of stability may help unravel some stochastic properties of these complex organizations, i.e., Lyapunov exponents, entropy, natural measure, etc., cf. Cvitanovic [1]. Stability and sensitivity calculations require robust and efficient numerical algorithms for their computation. Concerning uniquely the computation of the periodic orbits there exist two groups of methods: *local methods* which aim to determine a point of the periodic orbit and which is set as the

* Corresponding author.
E-mail address: fgiannetti@unisa.it (F. Giannetti).

https://doi.org/10.1016/j.jcp.2021.110403
0021-9991/

initial value for further integration, and *global methods* that aim to reconstruct the whole solution without time integration. Among local methods, one may find the direct integration of the governing equations and the shooting technique. The latter minimizes the distance to the periodic orbit via an iterative procedure, which leads to an improvement on the convergence rate with respect to the simple time integration. These methods, without further modifications, however, fail to compute unstable periodic orbits (UPO) and, in some cases, they are characterized by a low convergence rate. Some of the stabilization techniques applied to UPO are the recursive projection method (RPM) [2] or the residual recombination approach (BoostConv) [3]. Global methods, on the other hand, seek for direct representation of the sought solution on a given basis in a weighted residual approach. In this way, one may distinguish among trigonometric or orthogonal collocation, whose weight basis is composed of Dirac delta functions and its ansatz is either a Fourier or polynomial basis respectively, and Fourier–Galerkin or harmonic balance, whose weight and ansatz basis is composed of Fourier functions. Collocation methods are common in numerical continuation tools, such as AUTO [4] and MatCont [5,6], due to their robustness and generality. They are able to compute not only periodic solutions but also homoclinic or heteroclinic connections. Fourier–Galerkin uses trigonometric base functions as ansatz as well as weight functions. Fourier base functions possess interesting properties: they are by definition periodic, easy to compute, and provide rapid convergence whenever the solution is smooth.

Similarly, the stability of periodic orbits may be carried out in a local or global manner. In the local approach, the computation of Floquet multipliers is realized by a power iteration or Arnoldi algorithm via a matrix-free approach which reconstructs a faithful projection of the monodromy matrix. On the contrary, global methods directly reconstruct the monodromy matrix, either in the time or frequency domain, which generally allows more accurate results with faster convergence. The algorithm for the evaluation of sensitivity quantities is composed of two main building blocks: computation of a periodic solution and resolution of its direct and adjoint linear stability problems. Accordingly, efficient and simpler numerical techniques for the resolution of both problems imply faster and easier evaluations of sensitivity quantities. Such a constraint leads us to discard local methods due to their slow rate of convergence towards the periodic state. Furthermore, given that the nature of the orbit is periodic, every sensitivity equation shall also be. The periodicity requirement is critical in the calculation of accurate sensitivity maps, such as those computed by Giannetti et al. [7]. Therefore, a methodology that respects such a constraint seems a natural choice. The present study presents in a systematic manner the computation of stability and sensitivity of periodic solutions of discretizations of PDEs (resp. solutions to a system of ODE) via the Fourier–Galerkin method where the determination of its stability is carried out by Floquet or Hill's theory. Authors follow the new framework developed by Giannetti et al. [8] to investigate the sensitivity of periodic orbits. Giannetti et al. [8] studied the sensitivity of the three-dimensional secondary instability of the wake to a structural perturbation of the associated linear equations. The region of maximum coupling between the velocity components was found using the most unstable Floquet mode and its adjoint mode. The authors reported also the variation of this region in time by considering a structural perturbation that is impulsively applied in time at a given phase of the vortex-shedding process. The present approach can be considered an efficient and effective approximation of the framework proposed in Giannetti et al. [8,7].

The text is structured as follows: first, the methodology for the computation of a periodic orbit and the evaluation of its stability is introduced in section 2. The Fourier–Galerkin method is introduced in section 2.1 and section 2.2 is dedicated to the evolution equations with quadratic nonlinearities, e.g., Lorenz-like systems or Navier–Stokes equations. Floquet stability is reviewed in a general context in section 2.3, which is then particularized to the frequency domain in section 2.4. Sensitivity computations are later introduced in section 2.5. Section 2.6 addresses the numerical solution of the large algebraic systems in a parallel context via iterative methods. Finally, the study is concluded by some numerical examples. At first, we show the ability of the present methodology to track the route to chaos via period-doubling in the Lorenz system. Sections 3.2 and 3.3 are then dedicated to two fluid flow cases to discuss the performance of the methodology and to demonstrate the utility of sensitivity maps in the identification of physical instability mechanisms.

2. Methodology

2.1. Periodic boundary value problem

Let us start with a generic autonomous class of evolution equations of the form:

$$\mathbf{B}\frac{\partial \mathbf{q}}{\partial t} = \mathbf{F}(\mathbf{q}, \nu), \quad \mathbf{q}(t+T) = \mathbf{q}(t), \tag{1}$$

where $\mathbf{B}$ is a linear operator, $\mathbf{F}$ is a nonlinear operator on a Hilbert space X with inner product $\langle \cdot, \cdot \rangle$, and $\nu \in \mathbb{R}^p$ the set of parameters. In this way, both differential algebraic problems (DAE) and evolutionary partial differential equations (PDE) are included. Natural Hilbert spaces for the infinite-dimensional case are Sobolev spaces, see Kapitula and Promislow [9], whereas in finite dimensions we will generally consider $\mathbb{R}^n$. In the following, we assume that the nonlinear operator $\mathbf{F}$ is of quadratic type, i.e., $\mathbf{F}(\mathbf{q}) = \mathbf{L}\mathbf{q} + \mathbf{N}(\mathbf{q}, \mathbf{q})$, where $\mathbf{L}$ and $\mathbf{N}(\cdot, \cdot)$ are linear and quadratic nonlinear operators, respectively. This choice will be clear later in section 2.2, however note that many analytical functions can be recast in this way, see Guillot et al. [10].

2.2. The Fourier–Galerkin method for periodic boundary problems

The solution of eq. (1) is T-periodic. Therefore, it seems a natural choice to parametrize any T-periodic orbit $\mathbf{q}^*$, in a $t \mod T$ basis, i.e., a Fourier basis. For that purpose, let us consider the Fourier–Galerkin method, also denoted harmonic balance (HB) in the literature, cf. [11,12]. Fourier–Galerkin can be seen as a weighted residual approach for a periodic ansatz and weight functions. Fourier base functions present the advantage of being easy to compute and provide fast convergence in smooth cases.

We start our analysis by introducing the Fourier–Galerkin projection operator π_N onto the Fourier basis as follows:

$$\begin{aligned} &\pi_N : X \times \mathbb{R} \to X \times (\mathbb{Z}/(2N+1)\mathbb{Z}) \\ &\pi_N(\mathbf{q}) = \mathbf{q}_h(t) = \mathbf{q}_0 + \textstyle\sum_{n=1}^{N} \left[\mathbf{q}_{c,n}\cos(n\omega t) + \mathbf{q}_{s,n}\sin(n\omega t)\right] \\ &\quad = \underbrace{\left[\mathbf{q}_0, \mathbf{q}_{1,c}, \mathbf{q}_{1,s}, ..., \mathbf{q}_{N,c}, \mathbf{q}_{N,s}\right]}_{(\mathbf{Q}^{(\tau,N)})^T} \underbrace{\left[1, \cos(\omega t), \sin(\omega t), ..., \cos(N\omega t), \sin(N\omega t)\right]}_{\mathcal{F}_\mathbf{N}}, \end{aligned} \tag{2}$$

where $\mathbf{Q}^{(\tau,N)}$ are the $2N+1$ Fourier coefficients of the approximated solution $\mathbf{q}_h$ and $\mathcal{F}_N$ is the Fourier basis in sine/cosine components. The ansatz $\mathbf{q}_h(t)$ and its derivative are smooth T-periodic functions.

The residual is defined as the difference between the nonlinear and the time-derivative term, which is expressed as follows:

$$\begin{aligned} &\mathbf{r} : X \times \mathbb{R} \to X \times \mathbb{R} \\ &\mathbf{r}(\mathbf{q}, \tfrac{\partial \mathbf{q}}{\partial t}, t) = \mathbf{B}\tfrac{\partial \mathbf{q}}{\partial t} - \mathbf{F}(\mathbf{q}). \end{aligned} \tag{3}$$

Following the Fourier–Galerkin or Bubnov–Galerkin method in the Fourier basis, the governing equations of HB are obtained by integrating the truncated residual equations weighted by the Fourier basis over a period $T = \frac{2\pi}{\omega}$. The obtained residual is called the *truncated residual*:

$$\begin{aligned} &\hat{\mathbf{r}}_h : X \times (\mathbb{Z}/(2N+1)\mathbb{Z}) \to X \times (\mathbb{Z}/(2N+1)\mathbb{Z}) \\ &\hat{\mathbf{r}}_h(\mathbf{Q}_N, \omega) = \textstyle\int_0^{\frac{2\pi}{\omega}} \mathbf{r}_h(\mathbf{q}_h, \tfrac{\partial \mathbf{q}_h}{\partial t}, t)^T \mathcal{F}_N \, dt = \mathbf{0}, \end{aligned} \tag{4}$$

where

$$\mathbf{r}_h(\mathbf{q}_h, \frac{\partial \mathbf{q}_h}{\partial t}, t) = \mathbf{B}\frac{\partial \mathbf{q}_h}{\partial t} - \mathbf{F}(\mathbf{q}_h). \tag{5}$$

Equation (5) provides $2N+1$ equations for $2N+2$ unknowns in the autonomous case. Autonomous systems present a continuous symmetry, i.e., $\mathbf{q}(t+\xi)$ is also a periodic solution with an arbitrary ξ phase. The phase of the limit cycle remains to be fixed. This is usually done by imposing a condition at $t=0$, i.e., $g(\mathbf{q}, \frac{\partial \mathbf{q}}{\partial t}, 0) = 0$ or an orthogonality condition $\int_0^T \mathbf{F}(\mathbf{q}_h)^T \mathbf{q}_h dt = 0$. Equation (5) corresponds to balancing each harmonic individually, that is to have null Fourier coefficients of the truncated residual.

Fourier–Galerkin equations So far, the procedure to obtain a periodic orbit remains general. Now, without loss of generality, we shall consider the case where the nonlinear flow is of quadratic type. This constraint is far from being restrictive since many evolution problems can be recasted in this form, see Cochelin et al. [13] for the finite-dimensional case. Under these assumptions, eq. (5) takes the form:

$$\begin{aligned} 0 &= \mathbf{L}\mathbf{q}_0 + \mathbf{N}_0 \\ n\omega\mathbf{B}\mathbf{q}_{n,s} &= \mathbf{L}\mathbf{q}_{n,c} + \mathbf{N}_{n,c}, \quad n = 1, \dots, N \\ -n\omega\mathbf{B}\mathbf{q}_{n,c} &= \mathbf{L}\mathbf{q}_{n,s} + \mathbf{N}_{n,s}, \quad n = 1, \dots, N \\ g_h(\mathbf{q}_h) &= 0. \end{aligned} \tag{6}$$

For the sake of brevity, Fourier coefficients $\mathbf{N}_i$ are not developed as functions of $\mathbf{Q}^{(\tau,N)}$, see appendix A for an explicit description of these terms. Formally, eq. (6) will be denoted as:

$$\mathbf{0} = -\omega\tilde{\mathbf{B}}\mathbf{Q}^{(\tau,N)} + \tilde{\mathbf{L}}\mathbf{Q}^{(\tau,N)} + \tilde{\mathbf{N}}(\mathbf{Q}^{(\tau,N)}, \mathbf{Q}^{(\tau,N)}) = \tilde{\mathbf{r}}(\mathbf{Q}^{(\tau,N)}), \tag{7}$$

where operators $\tilde{\mathbf{B}}$, $\tilde{\mathbf{L}}$, and $\tilde{\mathbf{N}}(\cdot,\cdot)$ are detailed in appendix A and it is assumed that the phase of the limit cycle has been fixed.

Remark 1. It is here highlighted that if one desires to compute a $2T$-periodic solution $\tilde{\mathbf{q}}^*$, since a $2T$-periodic solution is also T-periodic, the current strategy requires some modifications. The methodology is adapted by doubling the number of harmonics to $2N$: the odd harmonics of the initial guess coincide with those of the T-periodic solution, and even modes are initialized to zero or to the Floquet mode associated with a period-doubling bifurcation, see section 2.4.

Finally, we briefly recall that Stokes [14] provided a dedicated theorem about the convergence of eq. (7). In particular, if the exact problem eq. (1) possesses a solution $\mathbf{q}^*$ of period $T = \frac{2\pi}{\omega}$, then the solution $[\mathbf{Q}^{\tau,N}, \omega^{\tau,N}]$ of the system eq. (7), for sufficiently large N, converges to the exact solution $\mathbf{q}^*$ if the monodromy matrix possesses a unique Floquet multiplier of multiplicity one.

Remark 2. In the original work of Stokes [14], where the theorem was originally proved, the main hypothesis was the *non-criticality* of the periodic solution, i.e., the periodic orbit is isolated in the phase space: the neutral Floquet multiplier is of multiplicity one.

2.3. Floquet-time stability theory

In this section, the Floquet theory of finite-dimensional systems in $\mathbb{R}^N$ is addressed. Unfortunately, there does not exist a general theory for time-periodic PDEs but some particular cases have been already tackled, see parabolic and hyperbolic evolution problems in Kuchement [15, Chapter 5] and references therein. For the sake of self-consistency, let us introduce a set of classical definitions in the study of dynamical systems.
For the sake of self-consistency, let us introduce a set of classical definitions in the study of dynamical systems.
Let $t \to \mathbf{q}^*(t)$ be a T-periodic solution of eq. (1) for a given set of parameters $\nu^* \in \mathbb{R}^p$. The associated *flow* of eq. (1) is denoted by $\varphi(t; \mathbf{q}_0)$, which solves $\mathbf{B}\frac{\partial \mathbf{q}}{\partial t} = \mathbf{F}(\mathbf{q}, \nu)$ with $\mathbf{q}(0) = \mathbf{q}_0$.
Furthermore, we consider a codimension one hypersurface S, chosen in such a way that every trajectory that crosses S in a neighborhood of the intersection point $\mathbf{o} \in S$ of the periodic orbit with the surface S intersects transversally and in the same direction, see Kuznetsov [16]. Such a section S is denoted as *Poincaré section*. Thanks to the Poincaré section, let us define the *Poincaré map* or *return map* $\mathbf{P}(\mathbf{o})$:

$$\mathbf{P}(\mathbf{o}) := \mathbf{P}_S(\mathbf{o}) = \varphi(T_S(\mathbf{o}); \mathbf{o}), \tag{8}$$

where $T_S(\mathbf{o})$ is the return time and it coincides with the period T of the periodic orbit when $\mathbf{o}^*$ is a fixed point, i.e., $\mathbf{o}^* = \mathbf{P}(\mathbf{o}^*)$:

$$\mathbf{o} \xrightarrow[\mathbf{q}\to\mathbf{q}^*]{} \mathbf{o}^* \quad \text{implies} \quad T_S(\mathbf{o}) \to T.$$

The linear stability of the T-periodic orbit $\mathbf{q}^*(t)$ can be studied by checking the evolution of the perturbed distance $\delta\mathbf{q}(t)$ to the T-periodic orbit $\mathbf{q}^*$:

$$\delta\mathbf{q}(t) = \varphi(t; \mathbf{q}^* + \delta\mathbf{q}_0) - \varphi(t; \mathbf{q}^*), \quad \text{with} \quad \delta\mathbf{q}(0) = \delta\mathbf{q}_0. \tag{9}$$

Measuring the distance after a period yields:

$$\delta\mathbf{q}(T) = \varphi(T; \mathbf{q}^* + \delta\mathbf{q}_0) - \varphi(T; \mathbf{q}^*) = \frac{\partial\varphi(T; \mathbf{q}^*)}{\partial\mathbf{q}}\delta\mathbf{q}_0 + O(||\delta\mathbf{q}_0||^2), \tag{10}$$

where in the last expression appears the *monodromy matrix* $\frac{\partial\varphi(T;\mathbf{q}^*)}{\partial\mathbf{q}}$. To find another representation of the monodromy matrix, consider the following evolution equation:

$$\mathbf{B}\frac{\partial}{\partial t}\frac{\partial\varphi(t; \mathbf{q}^*)}{\partial\mathbf{q}} = \frac{\partial\mathbf{F}(\varphi, \lambda^*)}{\partial\varphi}\frac{\partial\varphi(t; \mathbf{q}^*)}{\partial\mathbf{q}}, \quad \frac{\partial\varphi(0; \mathbf{q}^*)}{\partial\mathbf{q}} = \mathbf{I}. \tag{11}$$

Consequently, the monodromy matrix will be denoted by $\Phi(T) = \frac{\partial\varphi(T;\mathbf{q}^*)}{\partial\mathbf{q}}$, where the *fundamental solution matrix* $\Phi(t) \in \mathcal{M}(\mathbb{R})^{N\times N}$ satisfies the following matrix initial-value problem:

$$\mathbf{B}\frac{\partial\Phi}{\partial t} = \frac{\partial\mathbf{F}}{\partial\mathbf{q}}(\mathbf{q}^*, \lambda^*)\Phi, \quad \Phi(0) = \mathbf{I}. \tag{12}$$

The spectrum of the monodromy matrix is composed of an eigenvalue $\mu = 1$, due to the translation invariance of the periodic orbit and another set of $N-1$ eigenvalues. Due to the definition of the Poincaré map, it is not difficult to observe that the other $N-1$ eigenvalues of the Jacobian operator coincide with those of the derivative of the Poincaré map $DP(\mathbf{o}^*)$, see the book of Seydel [17] and references therein for a proof.

Thanks to Floquet's theorem, the perturbation $\delta\mathbf{q}(t)$ is written as:

$$\delta\mathbf{q}(t) = \sum_{n=1}^{N} c_n \delta\mathbf{q}_n(t),$$

where *fundamental solutions* $\delta\mathbf{q}_n$ can be rewritten in the Floquet's normal form:

$$\delta\mathbf{q}_n(t) = e^{\lambda_n t}\mathbf{p}_n(t), \tag{13}$$

where $\mathbf{p}_n$ is a T-periodic vector and λ_n are called the *Floquet exponents*. They are related to the eigenvalues μ_n of the monodromy matrix, also called *Floquet multipliers*, by the following relation: $\lambda_n = \frac{\log(\mu_n)}{T} + ik\omega$ for $k \in \mathbb{Z}$. To see this relation, consider linear independence of fundamental solutions and let us substitute the Floquet's normal form into eq. (10). Then, we are left with the following expression:

$$\mu_n \mathbf{p}_n(0) = \frac{\partial\varphi(T;\mathbf{q}^*)}{\partial\mathbf{q}}\mathbf{p}_n(0) \iff \lambda_n \mathbf{B}\mathbf{p}_n = \Big[-\mathbf{B}\frac{\partial}{\partial t} + \frac{\partial\mathbf{F}(\mathbf{q}^*,\lambda)}{\partial\mathbf{q}}\Big]\mathbf{p}_n. \tag{14}$$

2.4. Hill's method

In section 2.3, we have carried out a brief review of the stability of periodic orbits. Here, we aim to determine an efficient algorithm for the solution of the Floquet stability eq. (14). Prior to the discussion of the algorithm, please note the following analogy between the HBM parametrization of the autonomous problem eq. (1) and the Poincaré map, introduced in eq. (8). Phase condition may be interpreted as the parametrization of a codimension one hypersurface. Then, the T-periodic solution $\mathbf{q}_h^*$ taken at nT instants, $n \in \mathbb{N}$, is a fixed point of the Poincaré map. As discussed in section 2.3, eigenvalues of the derivative of the Poincaré map determine the stability of the periodic orbit, and these arise as a subproduct of the computation of the periodic orbit.

Nevertheless, this procedure to determine the Floquet stability would break the continuous symmetry, i.e., the phase is fixed, then the neutral Floquet multiplier, i.e., $\mu = 1$, would not be in the spectrum set. Therefore, in practice, the phase condition is left in the stability study.

The Fourier–Galerkin form of Floquet stability eq. (14) consists in the projection onto the finite Fourier space $X \times (\mathbb{Z}/(2N+1)\mathbb{Z})$, i.e., on a finite Fourier series.

The Floquet stability problem in the Fourier–Galerkin basis can be formally expressed with the following generalized eigenvalue problem:

$$\begin{aligned} \lambda^{(\tau,N)}\,\mathrm{diag}(\mathbf{B})_{2N+1}\mathbf{P}^{(\tau,N)} &= D\tilde{\mathbf{r}}(\mathbf{Q}^{(\tau,N)})\mathbf{P}^{(\tau,N)} \\ \text{where } D\tilde{\mathbf{r}}(\mathbf{Q}^{(\tau,N)})\mathbf{P}^{(\tau,N)} &= \Big[-\omega\tilde{\mathbf{B}} + \tilde{\mathbf{L}} + D\tilde{\mathbf{N}}(\mathbf{Q}^{(\tau,N)})\Big]\mathbf{P}^{(\tau,N)}, \end{aligned} \tag{15}$$

where $\mathbf{P}^{(\tau,N)} = \big[\mathbf{p}_0, \mathbf{p}_{1,c}, \mathbf{p}_{1,s}, ..., \mathbf{p}_{N,c}, \mathbf{p}_{N,s}\big]^T$ is the finite Fourier decomposition of the periodic eigenvector $\mathbf{p}(t)$ and $\lambda^{(\tau,N)}$ is the approximation of the Floquet exponent defined eq. (13).

Please note that the explicit definition of the derivative of the residual operator $D\tilde{\mathbf{r}}(\mathbf{Q}^{(\tau,N)})$ can be found in appendix A.

As depicted in Fig. 1, Floquet exponents are not unique in the complex field $\mathbb{C}$, nevertheless they are in $\mathbb{C}/i\omega\mathbb{R}$. Let us consider the finite-dimensional case, i.e., $\mathbf{q}^* \in \mathbb{R}^n$. In such a case, the Floquet spectrum is of dimension n, i.e., there are n eigenvalues in $\mathbb{C}/i\omega\mathbb{R}$. Nonetheless, the dimension of the Floquet HBM problem is $(2N+1)n$, there are $2N+1$ in the same conjugacy class, i.e., $\lambda_k^\tau = \lambda_0^\tau + ik\omega, k \in \mathbb{Z}$, where λ_0^τ is the eigenvalue closest to the real axis in the complex plane.

This remark motivates the definition of the *truncated spectra* Λ_N: this set of converged eigenvalues is a compact set in $\mathbb{C}$ restricted to the strip $C_\omega \equiv \{z \in \mathbb{C} : \omega/2 \le \mathrm{Im}(z) \le \omega/2\}$ (Fig. 2).

Notes on the convergence of the truncated spectra Since eq. (15) is a spectral approximation of the continuous problem eq. (10), an important aspect of the methodology is whether or not the eigenvalue λ and the eigenvector $\mathbf{P}_N$ converge to the actual eigenvalue and eigenmode respectively. Zhou et al. [18] have partially answered this query. They proved the convergence of the truncated problem in the strip $C_\omega \equiv \{z \in \mathbb{C} : \omega/2 \le \mathrm{Im}(z) \le \omega/2\}$ under the assumption that the nonlinear flow $F(\mathbf{q}, \nu)$ is piecewise $C^1[0,T]$. Likewise, Deconick et al. [19] proved the convergence of Hill's method in the Floquet–Bloch theory, i.e., periodicity in space, for compact subsets of $\mathbb{C}$. They proved the absence of spurious eigenvalues, i.e., an eigenvalue λ_n which does not converge to any eigenvalue λ of the problem eq. (14) as the number of harmonics $N \to \infty$. In the same reference, one may find for self-adjoint operators that for any eigenvalue λ of the monodromy operator, there exists a sequence $\{\lambda_N\}_{N=1}^{\infty}$ such that $\lim_{N\to\infty}|\lambda_N - \lambda| \to 0$ and with a spectral rate of convergence, i.e., $|\lambda_N - \lambda| = O(N^{-p})$ for $p \ge 1$, which has been later extended for a larger family of periodic differential operators by Jonshon et al. [20].

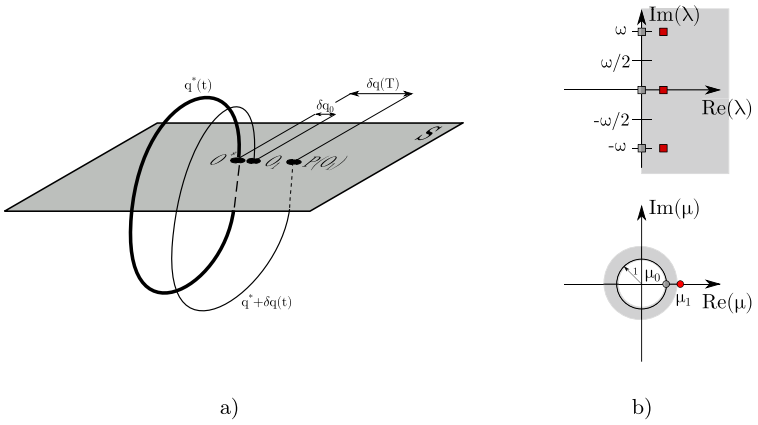

Fig. 1. a) An unstable periodic orbit $\mathbf{q}^*$ crossing the Poincaré section at point $\mathbf{o}^*$, and the evolution perturbed orbit $\mathbf{q}^* + \delta\mathbf{q}(t)$ from the point $\mathbf{o}_1$. b) Floquet spectrum in terms of Floquet multipliers μ_n (resp. Floquet exponents λ_n on top figure) of an unstable periodic orbit $\mathbf{q}^*$. Red dots (square on the top figure) are associated to the unstable fundamental solution $\delta\mathbf{q}_1(t)$ whereas gray markers denote the neutral Floquet eigenvalue. (For interpretation of the colors in the figure(s), the reader is referred to the web version of this article.)

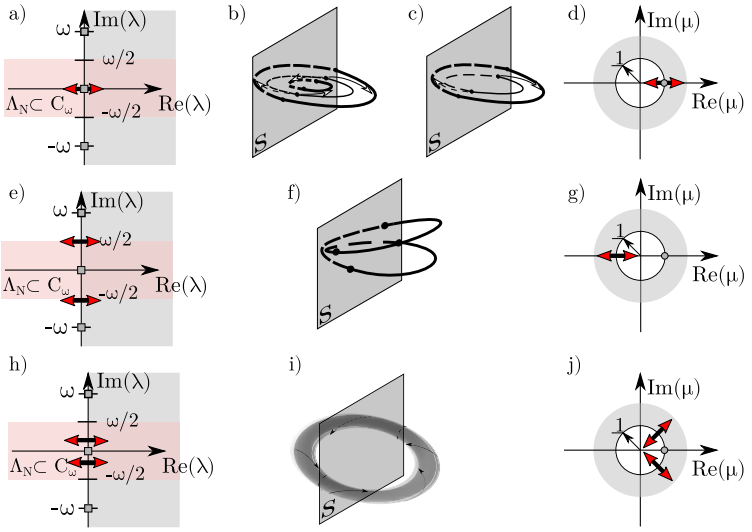

Fig. 2. Local bifurcations of codimension one of periodic orbits. Spectrum in terms of Floquet exponents a), e), and h). Spectrum in terms of Floquet multipliers d), g), and j). Pitchfork bifurcation in a), b), and d). Fold bifurcation in a), c), and d). Period-doubling bifurcation in e), f), and g). Neimark–Sacker in h), i), and j).

Finally, let us contemplate other choices for the selection of the set of converged eigenvalues. Bentvelsen et al. [21] compared different sorting algorithms to determine the set of converged eigenvalues and eigenmodes. They employed a sorting algorithm between elements in the same conjugacy class, i.e., $\lambda_n = \lambda_j + ik\omega$. Numerical experiments reported a faster numerical strategy to produce a set of converged eigenvalues, but such an approach is not yet rigorously justified. Such a sorting algorithm seems to be the preferred strategy for mechanical systems, see Lazarus et al. [22] and Guillot et al. [23].

For convenience, we introduce also the Floquet adjoint stability problem with respect to the natural inner product in the Fourier–Galerkin basis:

$$\begin{aligned} \bar{\lambda}^{(\tau,N)}\,\mathrm{diag}(\mathbf{B})_{2N+1}\mathbf{P}^{\dagger(\tau,N)} &= D\tilde{\mathbf{r}}^T(\mathbf{Q}^{(\tau,N)})\mathbf{P}^{\dagger(\tau,N)} \\ \text{where } D\tilde{\mathbf{r}}^T(\mathbf{Q}^{(\tau,N)})\mathbf{P}^{\dagger(\tau,N)} &= \Big[-\omega\tilde{\mathbf{B}}^T + \tilde{\mathbf{L}}^T + D\tilde{\mathbf{N}}^T(\mathbf{Q}^{(\tau,N)})\Big]\mathbf{P}^{\dagger(\tau,N)}, \end{aligned} \tag{16}$$

where $\mathbf{P}^{\dagger(\tau,N)} = \left[\mathbf{p}_0, \mathbf{p}^\dagger_{1,c}, \mathbf{p}^\dagger_{1,s}, \ldots, \mathbf{p}^\dagger_{N,c}, \mathbf{p}^\dagger_{N,s}\right]^T$ is the finite Fourier decomposition of the periodic adjoint eigenvector $\mathbf{p}^\dagger(t)$ and the conjugate eigenvalue $\bar{\lambda}^{(\tau,N)}$ is the approximation of the adjoint Floquet exponent.

2.5. Sensitivity analysis for periodic orbits

This section is an introduction to sensitivity computations near a bifurcation point of the periodic solution. Among possible applications to sensitivity theory, one may find passive control or identification of underlying physical mechanisms leading to the instability.
Let us consider the infinitesimal perturbed problem of eq. (1) with respect to the state variable $\mathbf{q}$:

$$\mathbf{B}\frac{\partial(\mathbf{q}^* + \delta\mathbf{q})}{\partial t} = \mathbf{F}(\mathbf{q}^* + \delta\mathbf{q}, \nu) + \delta\mathbf{H}(\mathbf{q}^* + \delta\mathbf{q}), \quad \mathbf{q}^*(t+T) = \mathbf{q}^*(t). \tag{17}$$

A force-feedback perturbation $\delta\mathbf{H}(\mathbf{q}^* + \delta\mathbf{q})$ leads to changes in dynamics. The original work of Giannetti et al. [8] analyzed the effect of a local force-feedback $\delta\mathbf{H}(\delta\mathbf{q})$. For that purpose, authors introduced the concept of *structural sensitivity* tensor S_s to the secondary instability, i.e., a bifurcation of the Poincaré map associated with a T-periodic solution, which is the extension of the structural sensitivity tensor of bifurcations from a steady-state solution, introduced by Giannetti et al. [24]. The structural sensitivity measures the variation of a Floquet exponent $\delta\lambda$ with respect to variations of the Floquet mode $\delta\mathbf{p}$. In a second article, the same authors [7] introduced the sensitivity to variations in the periodic orbit $\mathbf{q}^*$ itself. This tensor field is called *sensitivity to baseflow* variations, denoted as S_b. Analogously to the structural sensitivity, the sensitivity to baseflow variations measures the effect of a localized force-feedback $\delta\mathbf{H}(\mathbf{q}^*)$. This leads to a variation in the Floquet exponent $\delta\lambda$ with respect to variations of the periodic solution $\delta\mathbf{q}^*$. S_b is evaluated following a similar procedure to S_s. Nonetheless, one must take special care to ensure the uniqueness of S_b. Uniqueness is guaranteed by construction and the Fredholm alternative. For the sake of clarity, S_b will not be rigorously introduced because it would lead to another set of definitions to overcome this technical issue, the interested reader is referred to [7].

Instead, we have decided to introduce another interesting sensitivity map S_ω, the sensitivity map to frequency variations of the limit cycle, which measures the variation of the frequency (resp. period) of the periodic state with respect to the introduction of a localized feedback. Furthermore, in the present section, authors introduce the novel harmonic sensitivity map S_s^n (resp. S_ω^n), which measures the effect of a structural harmonic perturbation. This last set of maps provides new insights into the harmonic nature of the instability. Each sensitivity quantity is directly computed in the frequency domain.

Let us begin with the averaged structural sensitivity tensor $\bar{\mathsf{S}}_s$ of a Floquet exponent λ:

$$\bar{\mathsf{S}}_s(\mathbf{x}) = \frac{\int_t^{T+t} \mathbf{Mp}\otimes\mathbf{Mp}^\dagger \mathrm{d}t}{\int_t^{T+t}\int_\Omega \mathbf{Mp}\cdot\mathbf{Mp}^\dagger \mathrm{d}\mathbf{x}\mathrm{d}t}. \tag{18}$$

It is the operator whose contraction with a generic infinitesimal localized feedback operator in space provides: $\delta\lambda = \mathsf{C}_1 : \bar{\mathsf{S}}_s(\mathbf{x}_0)$, where $\delta\mathbf{H}(\delta\mathbf{q}) = \delta(\mathbf{x}-\mathbf{x}_0)\mathsf{C}_1\cdot\delta\mathbf{q}$, where $\delta(\mathbf{x}-\mathbf{x}_0)$ is the Dirac distribution at $\mathbf{x}-\mathbf{x}_0$ and C_1 is a generic constant feedback matrix. In the sensitivity paradigm, it is also helpful to consider phase details of the structural sensitivity which are retrieved by considering impulsive structural perturbations applied in time at a precise phase of the periodic solution, i.e., at $t = t_0$. This consideration leads to the instantaneous structural sensitivity S_s:

$$\mathsf{S}_s(\mathbf{x}, t) = \frac{\mathbf{Mp}\otimes\mathbf{Mp}^\dagger}{\int_t^{T+t}\int_\Omega \mathbf{Mp}\cdot\mathbf{Mp}^\dagger \mathrm{d}\mathbf{x}\mathrm{d}t}. \tag{19}$$

In such a case, the variation of the Floquet exponent $\delta\lambda = \mathsf{C}_1 : \mathsf{S}_s(\mathbf{x}_0, t_0)$, where $\delta\mathbf{H}(\delta\mathbf{q}) = \delta\big((t \mod T) - t_0\big)\delta\big(\mathbf{x}-\mathbf{x}_0\big)\mathsf{C}_1\cdot\delta\mathbf{q}$, provides access to the phase. However, it fails to determine the harmonic nature of the instability. For such considerations, it is helpful to introduce a novel sensitivity map, the harmonic structural sensitivity S_s^n, where n indicates the harmonic number. The direct computation of the frequency spectra S_s^n is in general complex-valued. However, for the sake of self-consistency with the previous methodology, $\mathsf{S}_s^{n,(s|c)}$ is the real harmonic structural sensitivity:

$$\begin{aligned}
\mathsf{S}_s^{n,c}(\mathbf{x}) &= \frac{2}{T}\frac{\int_t^{T+t} \mathbf{Mp}\otimes\mathbf{Mp}^\dagger \cos(n\omega t)\mathrm{d}t}{\int_t^{T+t}\int_\Omega \mathbf{Mp}\cdot\mathbf{Mp}^\dagger \mathrm{d}\mathbf{x}\mathrm{d}t} \\
\mathsf{S}_s^{n,s}(\mathbf{x}) &= \frac{2}{T}\frac{\int_t^{T+t} \mathbf{Mp}\otimes\mathbf{Mp}^\dagger \sin(n\omega t)\mathrm{d}t}{\int_t^{T+t}\int_\Omega \mathbf{Mp}\cdot\mathbf{Mp}^\dagger \mathrm{d}\mathbf{x}\mathrm{d}t},
\end{aligned} \tag{20}$$

where the structural perturbation $\delta\mathbf{H}(\delta\mathbf{q}) = \frac{2}{T}\cos(n\omega t)\delta\big(\mathbf{x}-\mathbf{x}_0\big)\mathsf{C}_1\cdot\delta\mathbf{q}$ (resp. $\sin(n\omega t)$) provides a variation of the Floquet exponent $\delta\lambda = \mathsf{C}_1 : \mathsf{S}_s^{n,c}(\mathbf{x}_0)$ (resp. $\mathsf{S}_s^{n,s}(\mathbf{x}_0)$) due to a harmonic perturbation. The $\frac{2}{T}$ term is simply a normalization factor.

Remark 3. In the original work of Giannetti et al. [8], $\mathbf{M} = \mathbf{B}$. The inclusion of the matrix $\mathbf{M}$ in the definition of the structural sensitivity was done to consider a particular set of variables instead of the whole set of variables. We highlight that definition eqs. (18) to (20) are valid for PDEs. Finite-dimensional systems do not depend on spatial coordinates. Therefore, there is no need to introduce a localized feedback force, i.e., $\delta\mathbf{H}(\delta\mathbf{q}) = \mathsf{C}_1\cdot\delta\mathbf{q}$.

The averaged structural sensitivity $\bar{\mathsf{S}}_s^{(\tau,N)}$ associated to the Floquet exponent $\lambda^{(\tau,N)}$ in the Fourier–Galerkin basis can be expressed as:

$$\bar{\mathsf{S}}_s^{(\tau,N)}(\mathbf{x}) = \frac{\mathbf{M}\mathbf{p}_0 \otimes \mathbf{M}\mathbf{p}_0^\dagger + \frac{1}{2}\sum_{n=1}^{N} \mathbf{M}\mathbf{p}_{n,c} \otimes \mathbf{M}\mathbf{p}_{n,c}^\dagger + \mathbf{M}\mathbf{p}_{n,s} \otimes \mathbf{M}\mathbf{p}_{n,s}^\dagger}{\int_\Omega \mathbf{M}\mathbf{p}_0 \cdot \mathbf{M}\mathbf{p}_0^\dagger + \frac{1}{2}\sum_{n=1}^{N} \mathbf{M}\mathbf{p}_{n,c} \cdot \mathbf{M}\mathbf{p}_{n,c}^\dagger + \mathbf{M}\mathbf{p}_{n,s} \cdot \mathbf{M}\mathbf{p}_{n,s}^\dagger \mathrm{d}\mathbf{x}}. \tag{21}$$

Analogously, harmonic components may be written as:

$$\begin{aligned}
\mathsf{S}_s^{n,c;(\tau,N)}(\mathbf{x}) = \; & \frac{2}{T\int_t^{T+t}\int_\Omega \mathbf{M}\mathbf{p}\cdot\mathbf{M}\mathbf{p}^\dagger \mathrm{d}\mathbf{x}\mathrm{d}t}\Big(\big[\mathbf{M}\mathbf{p}_{i,c} \otimes \mathbf{M}\mathbf{p}_0^\dagger + \mathbf{M}\mathbf{p}_0 \otimes \mathbf{M}\mathbf{p}_{i,c}^\dagger\big] \\
& + \tfrac{1}{2}\sum_{j=1}^{i-1}\big[\mathbf{M}\mathbf{p}_{i,c} \otimes \mathbf{M}\mathbf{p}_{i-j,c}^\dagger - \mathbf{M}\mathbf{p}_{j,s} \otimes \mathbf{M}\mathbf{p}_{i-j,s}^\dagger\big] \\
& + \tfrac{1}{2}\sum_{j=i+1}^{N}\big[\mathbf{M}\mathbf{p}_{j,c} \otimes \mathbf{M}\mathbf{p}_{j-i,c}^\dagger + \mathbf{M}\mathbf{p}_{j-i,s} \otimes \mathbf{M}\mathbf{p}_{j,s}^\dagger\big] \\
& + \tfrac{1}{2}\sum_{j=i+1}^{N}\big[\mathbf{M}\mathbf{p}_{j-i,c} \otimes \mathbf{M}\mathbf{p}_{j,c}^\dagger + \mathbf{M}\mathbf{p}_{j,s} \otimes \mathbf{M}\mathbf{p}_{j-i,s}^\dagger\big]\Big) \\
\mathsf{S}_s^{n,s;(\tau,N)}(\mathbf{x}) = \; & \frac{2}{T\int_t^{T+t}\int_\Omega \mathbf{M}\mathbf{p}\cdot\mathbf{M}\mathbf{p}^\dagger \mathrm{d}\mathbf{x}\mathrm{d}t}\Big(\big[\mathbf{M}\mathbf{p}_{i,s} \otimes \mathbf{M}\mathbf{p}_0^\dagger + \mathbf{M}\mathbf{p}_0 \otimes \mathbf{M}\mathbf{p}_{i,s}^\dagger\big] \\
& + \tfrac{1}{2}\sum_{j=1}^{i-1}\big[\mathbf{M}\mathbf{p}_{i,c} \otimes \mathbf{M}\mathbf{p}_{i-j,s}^\dagger + \mathbf{M}\mathbf{p}_{j,s} \otimes \mathbf{M}\mathbf{p}_{i-j,c}^\dagger\big] \\
& - \tfrac{1}{2}\sum_{j=i+1}^{N}\big[\mathbf{M}\mathbf{p}_{j,c} \otimes \mathbf{M}\mathbf{p}_{j-i,s}^\dagger + \mathbf{M}\mathbf{p}_{j-i,s} \otimes \mathbf{M}\mathbf{p}_{j,c}^\dagger\big] \\
& + \tfrac{1}{2}\sum_{j=i+1}^{N}\big[\mathbf{M}\mathbf{p}_{j-i,c} \otimes \mathbf{M}\mathbf{p}_{j,s}^\dagger + \mathbf{M}\mathbf{p}_{j,s} \otimes \mathbf{M}\mathbf{p}_{j-i,c}^\dagger\big]\Big).
\end{aligned} \tag{22}$$

In a similar fashion, let us introduce the sensitivity tensor of frequency variations ω, here denoted as $\bar{\mathsf{S}}_\omega$:

$$\bar{\mathsf{S}}_\omega(\mathbf{x}) = \frac{\int_0^T \mathbf{M}\mathbf{q}^* \otimes \mathbf{M}\mathbf{p}_h^\dagger \mathrm{d}t}{\int_0^T \int_\Omega \mathbf{M}\frac{\partial \mathbf{q}^*}{\partial t} \cdot \mathbf{M}\mathbf{p}_h^\dagger \mathrm{d}\mathbf{x}\mathrm{d}t}, \tag{23}$$

where $\mathbf{p}_h^\dagger$ is the adjoint Floquet mode associated to the neutral Floquet exponent $\lambda = 0$. $\bar{\mathsf{S}}_\omega$ is the operator whose contraction with a generic infinitesimal localized feedback operator in space provides the variation of the frequency $\delta\omega = \mathsf{C}_2 : \mathsf{S}_\omega$, where $\delta\mathbf{H}(\mathbf{q}^*) = \delta(\mathbf{x} - \mathbf{x}_0)\mathsf{C}_2 \cdot \mathbf{q}^*$.

The instantaneous sensitivity tensor to frequency variations S_ω is defined as:

$$\mathsf{S}_\omega(\mathbf{x}) = \frac{\mathbf{M}\mathbf{q}^* \otimes \mathbf{M}\mathbf{p}_h^\dagger \mathrm{d}t}{\int_0^T \int_\Omega \mathbf{M}\frac{\partial \mathbf{q}^*}{\partial t} \cdot \mathbf{M}\mathbf{p}_h^\dagger \mathrm{d}\mathbf{x}\mathrm{d}t}, \tag{24}$$

where $\delta\omega = \mathsf{C}_2 : \mathsf{S}_\omega(\mathbf{x}_\mathbf{0}, t_0)$ and $\delta\mathbf{H}(\delta\mathbf{q}) = \delta\big((t \mod T) - t_0\big)\delta\big(\mathbf{x} - \mathbf{x}_0\big)\mathsf{C}_2 \cdot \mathbf{q}^*$

Finally, let us introduce harmonic sensitivity to frequency variations maps $\mathsf{S}_\omega^{n,c}$ and $\mathsf{S}_\omega^{n,s}$. They provide further information for the open-loop control of the periodic solution with harmonic forcing. These quantities are a generalization of the weakly nonlinear expansion introduced by Sipp [25] to perform harmonic control near the onset of unsteadiness. These sensitivity maps are introduced as weighted products with the Fourier basis:

$$\begin{aligned}
\mathsf{S}_\omega^{n,c}(\mathbf{x}) &= \frac{2}{T}\frac{\int_0^T \mathbf{M}\mathbf{q}^* \otimes \mathbf{M}\mathbf{p}_h^\dagger \cos(n\omega t)\mathrm{d}t}{\int_0^T \int_\Omega \mathbf{M}\frac{\partial \mathbf{q}^*}{\partial t} \cdot \mathbf{M}\mathbf{p}_h^\dagger \mathrm{d}\mathbf{x}\mathrm{d}t} \\
\mathsf{S}_\omega^{n,s}(\mathbf{x}) &= \frac{2}{T}\frac{\int_0^T \mathbf{M}\mathbf{q}^* \otimes \mathbf{M}\mathbf{p}_h^\dagger \sin(n\omega t)\mathrm{d}t}{\int_0^T \int_\Omega \mathbf{M}\frac{\partial \mathbf{q}^*}{\partial t} \cdot \mathbf{M}\mathbf{p}_h^\dagger \mathrm{d}\mathbf{x}\mathrm{d}t},
\end{aligned} \tag{25}$$

where the structural perturbation $\delta\mathbf{H}(\delta\mathbf{q}) = \frac{2}{T}\cos(n\omega t)\delta\big(\mathbf{x} - \mathbf{x}_0\big)\mathsf{C}_2 \cdot \mathbf{q}^*$, resp. $\sin(n\omega t)$, provides a variation of oscillating frequency $\delta\omega = \mathsf{C}_2 : \mathsf{S}_\omega^{n,c}(\mathbf{x}_0)$, resp. $\mathsf{S}_\omega^{n,s}(\mathbf{x}_0)$, due to an harmonic perturbation. Eventually, the sensitivity of the frequency $\bar{\mathsf{S}}_\omega^{(\tau,N)}$ in the Fourier–Galerkin basis is computed as:

$$\bar{\mathsf{S}}_\omega^{(\tau,N)}(\mathbf{x}) = \frac{\mathbf{M}\mathbf{q}_0^* \otimes \mathbf{M}\mathbf{p}_{h;0}^\dagger + \frac{1}{2}\sum_{n=1}^{N} \mathbf{M}\mathbf{q}_{n,c}^* \otimes \mathbf{M}\mathbf{p}_{h;n,c}^\dagger + \mathbf{M}\mathbf{q}_{n,s}^* \otimes \mathbf{M}\mathbf{p}_{h;n,s}^\dagger}{\frac{\omega}{2}\int_\Omega \sum_{n=1}^{N} n\big[\mathbf{M}\mathbf{q}_{n,s}^* \cdot \mathbf{M}\mathbf{p}_{n,c}^\dagger - \mathbf{M}\mathbf{q}_{n,c}^* \cdot \mathbf{M}\mathbf{p}_{n,s}^\dagger\big]\mathrm{d}\mathbf{x}}, \tag{26}$$

and harmonic sensitivity tensors $\mathsf{S}_\omega^{n,c;(\tau,N)}$ and $\mathsf{S}_\omega^{n,s;(\tau,N)}$ in the Fourier–Galerkin basis:

$$
\begin{aligned}
\mathsf{S}_s^{n,c;(\tau,N)}(\mathbf{x}) = & \frac{2}{T\int_t^{T+t}\int_\Omega \mathbf{Mq}^*\cdot\mathbf{Mp}_h^\dagger \mathrm{d}\mathbf{x}\mathrm{d}t}\Big(\left[\mathbf{Mq}_{i,c}^*\otimes\mathbf{Mp}_{h;0}^\dagger+\mathbf{Mq}_0^*\otimes\mathbf{Mp}_{h;i,c}^\dagger\right] \\
& +\tfrac{1}{2}\textstyle\sum_{j=1}^{i-1}\left[\mathbf{Mq}_{i,c}^*\otimes\mathbf{Mp}_{h;i-j,c}^\dagger-\mathbf{Mq}_{j,s}^*\otimes\mathbf{Mp}_{h;i-j,s}^\dagger\right] \\
& +\tfrac{1}{2}\textstyle\sum_{j=i+1}^{N}\left[\mathbf{Mq}_{j,c}^*\otimes\mathbf{Mp}_{h;j-i,c}^\dagger+\mathbf{Mq}_{j-i,s}^*\otimes\mathbf{Mp}_{h;j,s}^\dagger\right] \\
& +\tfrac{1}{2}\textstyle\sum_{j=i+1}^{N}\left[\mathbf{Mq}_{j-i,c}^*\otimes\mathbf{Mp}_{h;j,c}^\dagger+\mathbf{Mq}_{j,s}^*\otimes\mathbf{Mp}_{h;j-i,s}^\dagger\right]\Big) \\
\mathsf{S}_s^{n,s;(\tau,N)}(\mathbf{x}) = & \frac{2}{T\int_t^{T+t}\int_\Omega \mathbf{Mq}^*\cdot\mathbf{Mp}_h^\dagger \mathrm{d}\mathbf{x}\mathrm{d}t}\Big(\left[\mathbf{Mq}_{i,s}^*\otimes\mathbf{Mp}_{h;0}^\dagger+\mathbf{Mq}_0^*\otimes\mathbf{Mp}_{h;i,s}^\dagger\right] \\
& +\tfrac{1}{2}\textstyle\sum_{j=1}^{i-1}\left[\mathbf{Mq}_{i,c}^*\otimes\mathbf{Mp}_{h;i-j,s}^\dagger+\mathbf{Mq}_{j,s}^*\otimes\mathbf{Mp}_{h;i-j,c}^\dagger\right] \\
& -\tfrac{1}{2}\textstyle\sum_{j=i+1}^{N}\left[\mathbf{Mq}_{j,c}^*\otimes\mathbf{Mp}_{h;j-i,s}^\dagger+\mathbf{Mq}_{j-i,s}^*\otimes\mathbf{Mp}_{h;j,c}^\dagger\right] \\
& +\tfrac{1}{2}\textstyle\sum_{j=i+1}^{N}\left[\mathbf{Mq}_{j-i,c}^*\otimes\mathbf{Mp}_{h;j,s}^\dagger+\mathbf{Mq}_{j,s}^*\otimes\mathbf{Mp}_{h;j-i,c}^\dagger\right]\Big).
\end{aligned}
\tag{27}
$$

2.6. Numerical methods

This section presents strategies for the resolution of eqs. (7) and (15). Efficient numerical techniques are required for the solution of linear systems composed of a large number of degrees of freedom. In particular, direct factorization becomes rapidly unfeasible due to the large memory requirements. Iterative methods with inner-outer preconditioning are proposed. Outer preconditioning improves the convergence of the Krylov method and inner preconditioning increases the efficiency of computation on blocks.

Nonlinear problem eq. (7) The solution of eq. (7) is performed via a Newton-like method:

$$
D\tilde{\mathbf{r}}(\mathbf{Q}_{(n)}^{(\tau,N)})\delta\mathbf{Q}_{(n+1)}^{(\tau,N)} = -\tilde{\mathbf{r}}(\mathbf{Q}_{(n)}^{(\tau,N)}). \tag{28}
$$

A Newton–Krylov strategy is chosen in the case $\tilde{\mathbf{r}}$ arises from semi-discretization in space of a PDE or via a Newton method if $\tilde{\mathbf{r}}$ is the vector field that stems from a differential system with a small number of degrees of freedom. The latter is common in the literature of mechanical systems and it is solved with dense matrices and direct linear solvers, for more information, the interested reader is referred to Krack et al. [12, Chapter 4].

Eigenvalue problem Arnoldi or shift-and-invert iteration are the chosen candidates for efficient extraction of leading Floquet exponents in eqs. (15) and (16).

Linear systems Preconditioning strategies are needed for an efficient resolution of linear systems from Newton iterations eq. (28) or Arnoldi iterations applied to eqs. (15) and (16). In the present study, we have considered three strategies for the outer preconditioning: block Jacobi, upper and lower triangular Gauss–Seidel. Solutions of inner systems, i.e., involving diagonal blocks of $D\tilde{\mathbf{r}}(\mathbf{Q}_{(n)}^{(\tau,N)})$, are computed using exact LU factorizations or iterative solvers, e.g., additive Schwarz method (ASM). For other choices of inner block-factorization, the interested reader may consider, for example, the modified augmented Lagrangian method [26] as implemented by Moulin et al. [27]. The preconditioning step is coupled with an iterative Krylov method: the flexible GMRES [28].

3. Results

Numerical results presented in this section have been obtained with in-house codes. Results presented in section 3.1 have been calculated with a MATLAB code developed by the authors for the computation of limit cycles and the evaluation of their stability with the methodology shown in section 2. Numerical examples of sections 3.2 and 3.3 have been computed with FreeFEM, a finite element code for the resolution of PDEs in the variational form, cf. [29]. Navier–Stokes equations written in the weak formulation are discretized by projecting the flow field (u, v, p) upon a basis of Taylor–Hood finite elements with piecewise quadratic velocities and piecewise linear pressure. The number of triangles of the discretized domain considered in sections 3.2 and 3.3 varies in a range of $\mathcal{O}(10^4)-\mathcal{O}(10^5)$ which results in around $\mathcal{O}(10^5)-\mathcal{O}(10^6)$ degrees of freedom per mode, that is $\mathcal{O}(n\cdot 10^5)-\mathcal{O}(n\cdot 10^6)$ with $n=2N+1$ the number of modes retained in the Fourier basis. Linear systems and eigenvalue problems are solved by PETSc [30] and SLEPc [31]. For more information, the interested reader is referred to the recent review article in linear and nonlinear stability in fluid flows by Fabre et al. [32] and the StabFem project hosted at https://stabfem.gitlab.io/StabFem/. Results presented in section 3.1 provide numerical evidence of the capability of the Fourier–Galerkin methodology to continue stable and unstable branches of periodic solutions past period-doubling bifurcations and to accurately evaluate the stability of a periodic orbit. Evaluation of the performance of numerical techniques described in section 2.6 and an assessment of the accuracy of sensitivity quantities

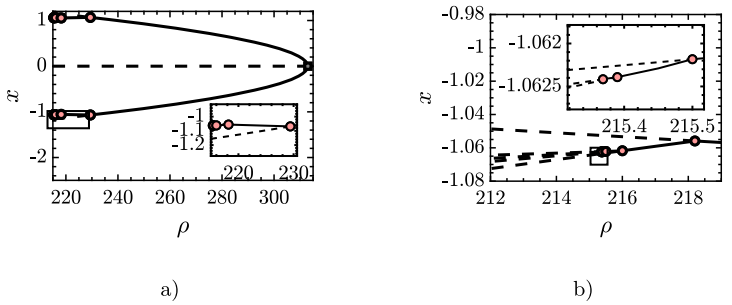

Fig. 3. a) Bifurcation diagram of the Lorenz system. b) Zoom into the interval of period-doubling bifurcations. Solid (resp. dashed) lines denote stable (resp. unstable) solutions. Red (resp. gray) markers denote a period-doubling bifurcation (resp. symmetry breaking).

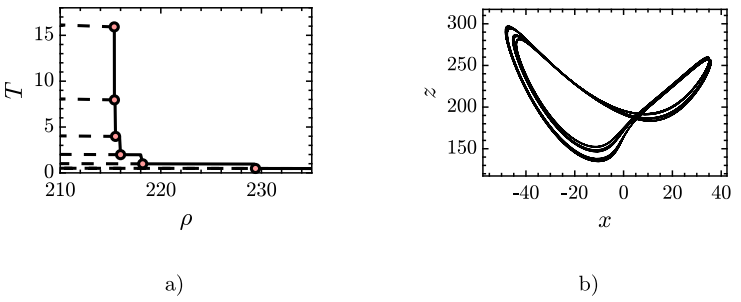

Fig. 4. a) Evolution of the period. b) $x-z$ slice of the stable solution at $\rho = 215.38$, before the sixth period-doubling bifurcation. Same legend as in Fig. 3.

detailed in section 2.5 is carried out in sections 3.2 and 3.3. The authors would like to compare the present methodology with respect to classical time-stepping techniques for the computation of sensitivity maps as in Giannetti et al. [7]. For that purpose, we consider an IMEX time-integration technique, e.g., explicit Runge–Kutta integration for the nonlinear terms and implicit Crank-Nicolson for the linear terms. The computation of the converged periodic solution, the direct and adjoint modes with time-stepping techniques require the solution of around $\mathcal{O}(MT)$ time units, with M the number of periods required for convergence, which is usually of the order of few hundreds for the periodic solution and of thousands for the evaluation of the direct and adjoints modes to obtain accurate results, and T the fundamental period. The evaluation of a period usually requires a number of time steps of the order of $N = \mathcal{O}(T/\Delta t)$, which is $N = \mathcal{O}(10^2)$ in the case of the wake flow past a cylinder, see [3, Sec. 7]. That results in a much larger total computation time than the one required for the evaluation of sensitivity maps with the current methodology. For instance, if we consider a coarse numerical domain, the mesh $\mathcal{M}_1$ of Table 1, the serial evaluation of Fourier–Galerkin methodology for the periodic solution, direct and adjoint eigenmodes are of the order of few minutes whereas the time-stepping methodology takes several hours, which is highly dependent on the time step which at the same time depends on the level of refinement. During the elaboration of this manuscript authors have compared the sensitivity maps computed with time-stepping techniques and Fourier–Galerkin method. Even if it is difficult to compare results that are coming from different numerical discretizations and different grids, [8] employed finite differences with a staggered grid, comparing the results we found that the sensitivity maps agree very well and the relative error is of few percents depending on the mesh and the physical parameters.

3.1. Lorenz system: the case of Feigenbaum route to chaos

Routes to chaos are of fundamental interest in the study of nonlinear dynamics. Most common routes to chaos are intermittency, crisis, quasiperiodicity, and period-doubling. The current section focuses on the latter. Period-doubling route is also denoted as *Feigenbaum* route to chaos and is characterized by an infinite number of period-doubling bifurcations in a finite interval of the parameter set. In particular, Feigenbaum noted that under mild assumptions of the nonlinear operator, the distance between consecutive bifurcations shrinks in a universal manner, see Collet et al. [33]:

$$\lim_{n\to\infty} \frac{\nu_{n+1} - \nu_n}{\nu_n - \nu_{n-1}} = \delta,$$

where $\delta \approx 4.6692016\ldots$ is the Feigenbaum constant for dissipative dynamical systems and it can be numerically evaluated from Figs. 3 and 4. Period-doubling arises as a pitchfork bifurcation of a fixed point of the associated Poincaré return map.

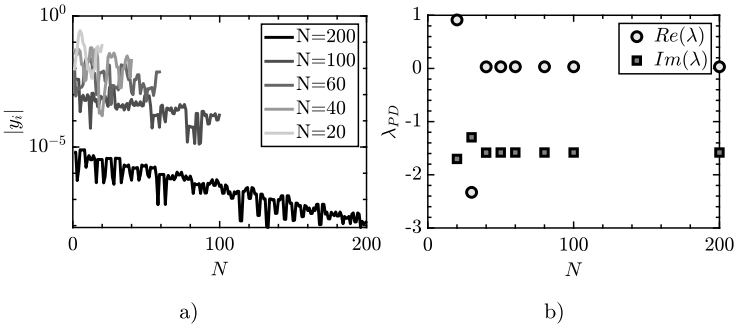

Fig. 5. a) Decay of Fourier modes of y component for a periodic solution near the fourth period-doubling bifurcation. b) Evolution of the eigenvalue associated to the period-doubling mode.

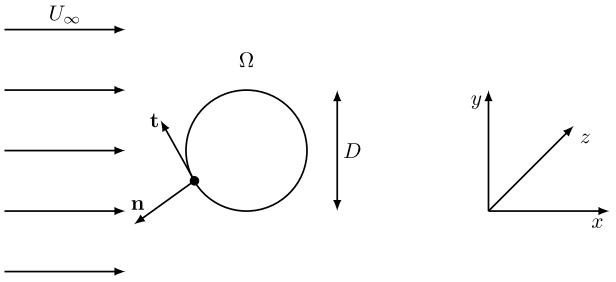

Fig. 6. Sketch of a cylinder immersed in a uniform flow.

In particular, here the Lorenz system illustrates the capability of the Fourier–Galerkin method to track period-doubling bifurcations and compute periodic solutions in a substantially nonlinear system. Let us first introduce Lorenz equations:

$$\begin{aligned} \dot{x} &= \sigma(y - x) \\ \dot{y} &= \rho x - y - xz \\ \dot{z} &= xy - bz, \end{aligned} \tag{29}$$

with parameters $b = \frac{8}{3}$, $\sigma = 10$, and $\rho \in (210, 320]$. In this range of parameters, there is a first bifurcation around $\rho \approx 312.9$, where the stable solution ceases to be symmetric via a pitchfork bifurcation due to the reflectional symmetry ($x \to -x$, $y \to -y$) of the system. These two branches remain stable up to $\rho \approx 229.4$, where a first period-doubling bifurcation occurs. It is then followed by an infinite number of them, of which the first six have been computed, see Fig. 3. The stable periodic orbit before the sixth period-doubling bifurcation is reported in Fig. 4 b). Fig. 4 a) illustrates the geometric growth of the period past successive period-doubling bifurcations. As pointed out in Remark 1, successive period-doubling solutions have been computed by doubling the number of harmonics of the truncated Fourier series.

The convergence of a periodic solution is evaluated a posteriori by the decay of Fourier modes and by the evolution of the leading eigenvalue. Fig. 5 shows, for a periodic solution at the onset of the fourth period-doubling bifurcation, the irregular decay of Fourier harmonics due to the strong nonlinearities. In addition, Fig. 5 shows that the methodology is able to accurately predict some parts of the spectrum even if the decay of Fourier modes is not smooth. Particularly, prior to the fourth period-doubling bifurcation Fig. 5, a minimum of around $N = 40$ is required for a correct evaluation of the leading Floquet exponent.

Finally, let us conclude this section with a remark concerning the number of Fourier modes retained for the reconstruction of a periodic solution past a period-doubling bifurcation. As stated in Remark 1, a periodic solution whose period is $2^m T$, i.e., the system has experienced m period-doubling bifurcations, is also $2^{m-1}T$-periodic. The computation of a $2^m T$-periodic solution requires $2^m \tilde{N}$ Fourier modes, where $\tilde{N}$ is the length of the Fourier basis used for the computation of a T-periodic solution. As a consequence, the number of harmonics for a single T-period is $\tilde{N} = \frac{N}{2^m}$, which, for instance for $N = 40$ and $m = 3$, gives $\tilde{N} = 5$.

3.2. Flow past a two-dimensional circular cylinder

Let us consider a fluid mechanics example: a canonical case of the flow past a bluff body, i.e., the flow past a two-dimensional cylinder sketched in Fig. 6. Dynamics and the first two bifurcations are well known, see Williamson [34].

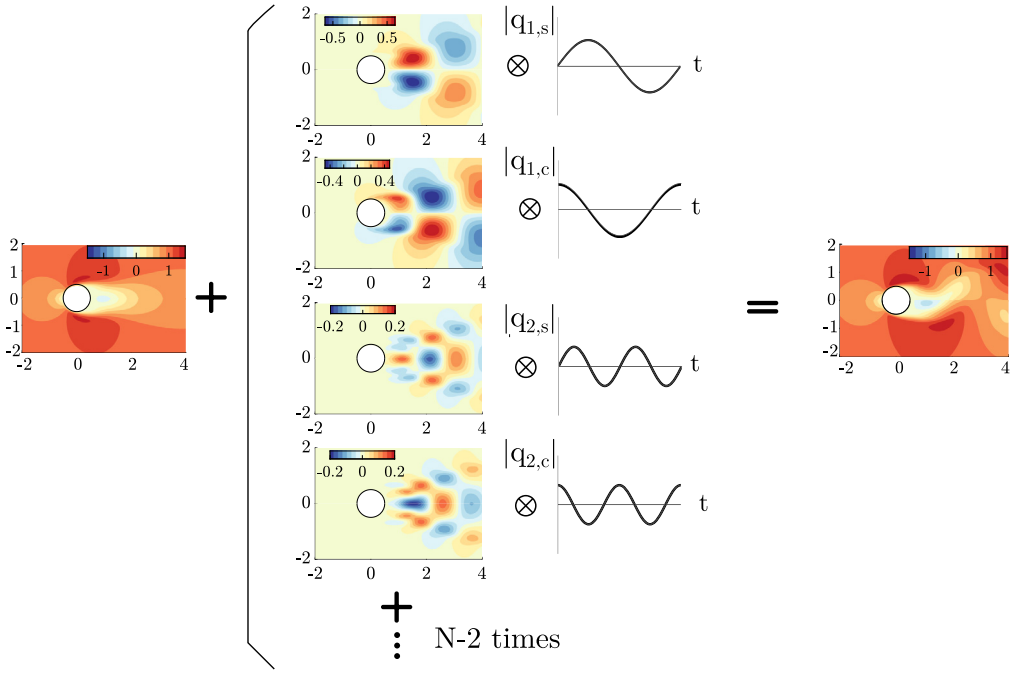

Fig. 7. Reconstruction of the streamwise velocity U_x of the periodic oscillating vortex solution at $Re = 190$. The flow is reconstructed at $t = 0$ for $N = 6$.

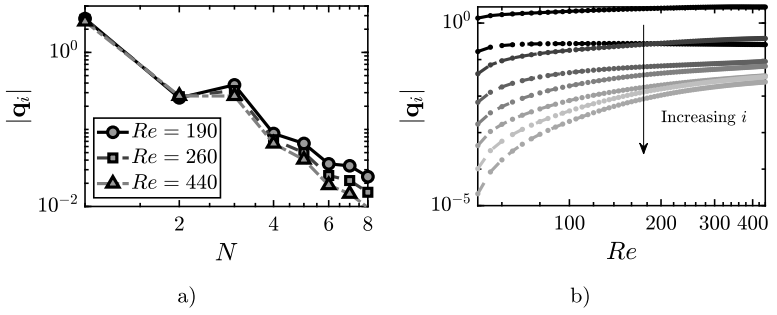

Fig. 8. a) Decay of Fourier spectrum for $Re = 190$, $Re = 260$, and $Re = 440$ b) Evolution of the amplitude of Fourier modes.

The governing equations are the incompressible Navier–Stokes equations which are of quadratic type, see appendix B, therefore they fit into the developed strategy.

3.2.1. Computation of the baseflow

The Fourier–Galerkin strategy reconstructs the periodic solution of the flow past a cylinder, as reported in Fig. 7. The approach is initialized with the unstable eigenmode at the threshold, $Re \approx 47$, and it is continued up to $Re = 450$, with at most $N = 10$ modes. In order to estimate the precision of the results obtained by the numerical procedure, two Reynolds numbers are selected, $Re = 190$ and $Re = 260$, and we run cross-comparison of the estimated Strouhal with the data available in the literature. At $Re = 190$ (resp. $Re = 260$), by retaining $N = 5$ harmonics, a Strouhal number $St = 0.1938$ (resp. $St = 0.2058$) has been obtained, a result in good agreement with the value $St = 0.1950$ (resp. $St = 0.2071$) reported by Barkley et al. [35]. These accurate results with a reduced Fourier basis are due to the rapid decay of the Fourier spectrum, which is displayed in Fig. 8 a). The Fourier spectrum displays a quadratic decay, with small dependence on the Reynolds number if sufficient modes are retained. To determine whether or not the number of retained modes is sufficient, one could evaluate a posteriori the evolution of the amplitude of each mode with respect to the parameter, i.e., Re. The amplitude of each Fourier mode grows exponentially until saturation, see Fig. 8 b). Therefore, an appropriate selection of N could be to retain at least a mode that is not saturated or select the basis length N so that the amplitude of the last mode is below a certain threshold.

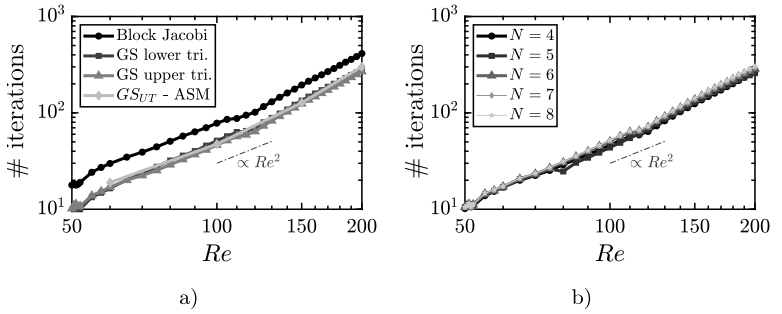

Fig. 9. Effect of Reynolds number, preconditioning technique and number of Fourier modes. a) Compares preconditioning techniques and b) the number of Fourier modes for a Gauss–Seidel upper triangular preconditioner.

Table 1
Average number of GMRES iterations per Newton iteration for three numerical domains $\mathcal{M}_1$, $\mathcal{M}_2$ and $\mathcal{M}_3$ at $Re = 100$ with upper triangular Gauss–Seidel. The tolerance of the Newton method is set to 10^{-8}.

Mesh ID	# elements	# GMRES iterations		
		$N = 1$	$N = 2$	$N = 3$
$\mathcal{M}_1$	$1.4 \cdot 10^4$	33	36	38
$\mathcal{M}_2$	$4.5 \cdot 10^4$	32	37	39
$\mathcal{M}_3$	$1.85 \cdot 10^5$	33	38	38

Table 2
Total number of GMRES iterations for the resolution of the nonlinear problem eq. (7) at $Re = 100$, $N = 4$ with the numerical domain $\mathcal{M}_1$, the upper triangular Gauss–Seidel as the outer preconditioning technique and inexact factorization with the ASM method for inner blocks. Variation of inner iterations and total GMRES iterations with respect to the relative tolerance in the inexact factorization of inner blocks. The tolerance of the Newton method is set to 10^{-8}.

ASM tolerance	10^{-8}	10^{-7}	10^{-6}	10^{-5}	10^{-4}	10^{-3}	LU
# total iterations	344	310	278	246	267	369	238
Average # inner iterations	52	44	35	25	18	16	–

3.2.2. Performance evaluation of iterative methods

Another important aspect to be addressed is the performance of methods used for numerical resolution. In particular, for the present case, authors have evaluated the dependency of the chosen iterative strategy, a flexible restarted GMRES, for the solution of linear systems such as eq. (28) on a set of parameters: Reynolds number, number of elements in the numerical domain, preconditioning techniques and number of modes of the Fourier basis.

Independently of the chosen preconditioning technique, the number of GMRES iterations for the resolution of the linear system eq. (28) increases quadratically with respect to the Reynolds number, see Fig. 9 a). As expected, triangular Gauss–Seidel preconditioning speeds up computations with respect to block Jacobi. However, the gain between choosing an upper or a lower triangular preconditioner is marginal. The second aspect that was studied is the influence of the number of iterations required to solve the linear system under a change of the total number of elements. Table 1 reports the average number of GMRES iterations, for three numerical domains $\mathcal{M}_i$, $i = 1, 2, 3$. It results that the number of GMRES iterations does scale with the total number of elements in the numerical domain. In addition, authors have studied the effect of an inexact factorization of the inner diagonal blocks. ASM is used to precondition the inner blocks with upper triangular GS as outer preconditioner. It is compared with exact LU factorization for the diagonal blocks. Table 2 reports the variation of the total number of GMRES iterations required to solve the nonlinear problem eq. (7) and the averaged number of inner iterations for each inner diagonal block. It is concluded that inexact factorization of inner blocks hardly changes the number of GMRES iterations, as long as the relative tolerance is correctly tuned. The effect of the number of modes in the truncated Fourier basis is reported in Fig. 9 b). Similar conclusions can be drawn with respect to other preconditioners, the number of modes in the Fourier basis does not affect the iterative strategy, as long as N is sufficient for convergence.

Finally, the performance of the parallel implementation is considered. For that purpose a strong scalability test has been carried out with a fine numerical domain composed of $1.85 \cdot 10^5$ elements. The number of modes is fixed to $N = 4$ and the preconditioning technique is the upper triangular Gauss–Seidel. Fig. 10 a) reports the evolution of the averaged time per Newton iteration with respect to the number of processes. The actual scaling time is degraded by around 35% with respect to perfect linear scaling, that is the average time per Newton iteration approximately evolves as # of processes$^{-0.65}$.

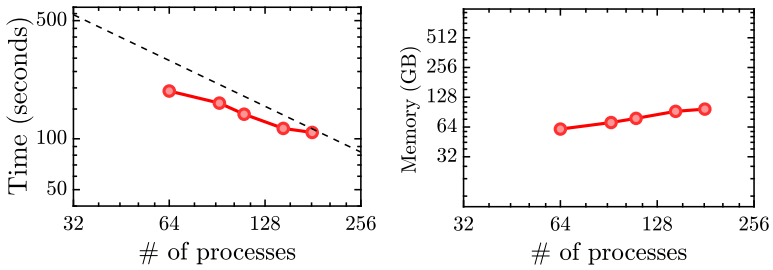

a) Average time per Newton iteration

b) Average memory consumption for the solution of eq. (28) in the Newton iteration.

Fig. 10. Performance of the linear solver with upper triangular Gauss–Seidel with a discretized domain composed of $1.85 \cdot 10^5$ elements and $N = 4$.

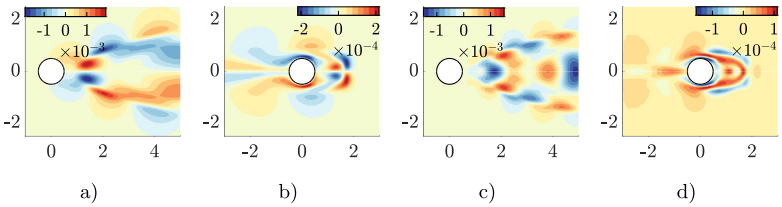

Fig. 11. Spanwise velocity component U_z of *mode A* at $Re = 190$. a) and c), resp. b) and d), first and second sinus components of direct, resp. adjoint, Floquet modes.

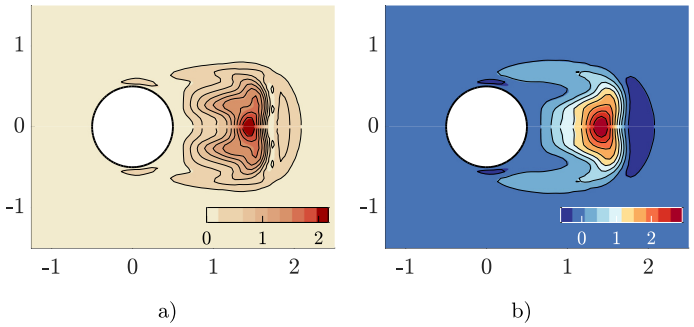

Fig. 12. Averaged structural sensitivity $\bar{S}_s^{(\tau,N)}$ of mode A at $Re = 190$, $k_z = 1.585$, and $N = 4$. a) Spectral norm. b) Trace.

Similarly, Fig. 10 b) reports the total memory consumption for the solution of the linear system eq. (28). It displays an increase of memory of around 20% each time the number of processes doubles.

In conclusion, GMRES iterations depend quadratically on Reynolds number and they are independent on the total number of mesh elements, the dimension of the Fourier basis as long as N is sufficient to characterize the periodic solution. In a future study, authors will study other preconditioning techniques to attempt to reduce the dependency on Re.

3.2.3. Stability & sensitivity analysis

Beyond the threshold of the first instability, which is found at around $Re \approx 47$, a stable two-dimensional T-periodic solution exists up to $Re \approx 190$ where the stable solution ceases to be two-dimensional via a steady symmetry-breaking bifurcation of the spanwise homogeneous direction. The Floquet mode associated to this second instability, reported in Fig. 11, is commonly denoted as *mode A* whose wavenumber is $k_z = 1.585$, see Giannetti et al. [8].

Prior to the discussion of sensitivity quantities, let us point out their validity. The reported sensitivity maps in Figs. 12 and 13 are in perfect agreement with those presented in literature, cf. [7]. A common query in physics is: which are the underlying physical mechanisms responsible for the instability? Structural sensitivity allows to localize the core of the vortex-shedding instability, that is the sensitivity of the Floquet exponent to a generic structural perturbation of the linearized equations. Fig. 12 displays the compact support structure of the sensitivity for mode A, which translates to a localized instability in the near wake. Similarly, if one desires to shift the harmonic frequency ω, the most efficient way is to act on the near wake in accordance with the map S_ω, see Fig. 13.

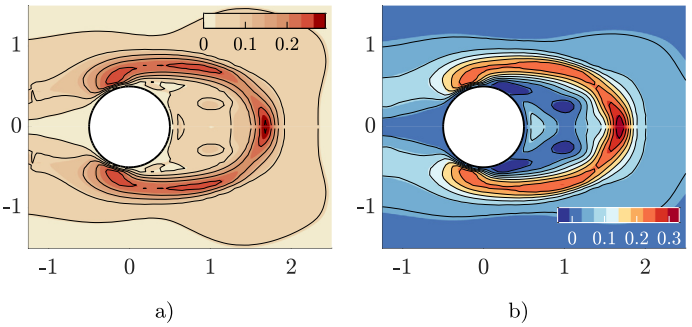

Fig. 13. Averaged sensitivity to frequency variations $\bar{S}_{\omega}^{(\tau,N)}$ of mode A at $Re = 190$, $k_z = 1.585$, and $N = 4$. a) Spectral norm. b) Trace.

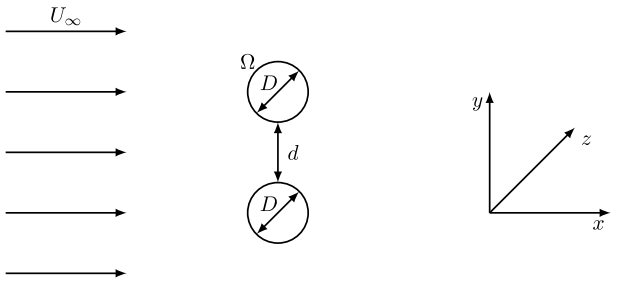

Fig. 14. Sketch of the two circular cylinders in a side-by-side arrangement immersed in a uniform flow.

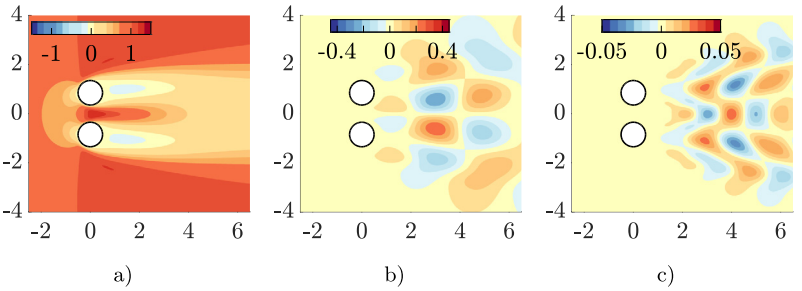

Fig. 15. Streamwise component U_x of the periodic baseflow solution at $Re = 62$. a) Meanflow component. b) First cosinus component. c) Second cosinus component.

3.3. Flow past two cylinders in tandem

Let us explore a second fluid mechanics example: the flow past two side-by-side circular cylinders. The flow configuration, reported in Fig. 14, is governed by two dimensionless parameters, Reynolds number (Re) and the ratio of the distance between cylinders and their diameter ($g = \frac{d}{D}$). For some ranges of parameters, reported by Carini et al. [36], the two-dimensional flow pattern is characterized by an asymmetric unsteady wake with respect to the horizontal axis. Such a phenomenon, which has been denominated *flip-flop*, develops at low Reynolds numbers, $50 < Re < 90$, through a Neimark–Sacker bifurcation. In the following, the dimensionless distance between cylinders is fixed, $g = 0.7$, such that *flip-flop* instability appears.

3.3.1. Computation of the baseflow

The periodic solution past two side-by-side cylinders is reconstructed by Fourier–Galerkin with $N = 4$ (Fig. 15). The method is initialized with the unstable in-phase eigenmode associated with the first supercritical Hopf bifurcation of the steady state, see section 3.2.3. The accuracy of baseflow computations were compared with reported results in the literature. At $Re = 62$, a $St \approx 0.111$ matches the one computed by Carini et al. [36].

3.3.2. Memory requirements of linear solvers

Section 3.2.2 focuses on the performance of iterative methods by considering the influence of some parameters on the number of iterations required by the linear solver to solve eq. (28) with a relative tolerance of 10^{-5}. Another important facet of linear solvers is their memory consumption. Particularly, the total memory consumption is expected to increases with

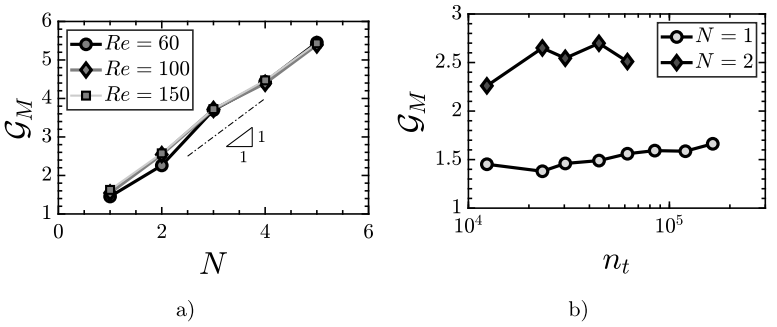

Fig. 16. a) Memory gain evolution w.r.t. number of Fourier modes (for a coarse mesh $n_t = 12354$ triangles) for three Reynolds numbers. b) Memory gain w.r.t. number of mesh triangles.

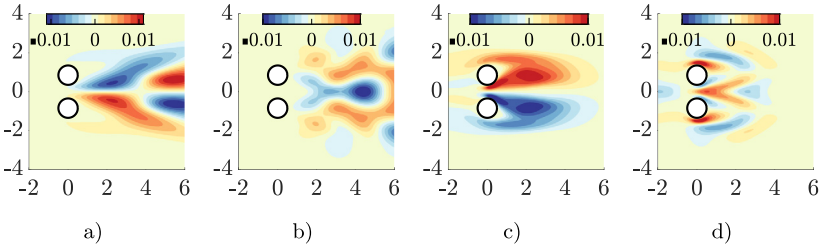

Fig. 17. *Mode IP* at $Re = 62$. a) and c), resp. b) and d), meanflow and first cosinus components of direct, resp. adjoint, Floquet modes.

the number of modes of the truncated Fourier basis and mesh refinement. We define the *memory gain*, $\mathcal{G}_M = \frac{\text{memory LU}}{\text{memory GMRES}}$, as the ratio of memory consumed by LU w.r.t. GMRES to solve a linear system whose linear operator is the Jacobian matrix defined in appendix A.3.

Tests have been run on an Intel cluster with 64 Intel(R) Xeon(R) CPU E5-4610 processors and 256 GB of memory. For a fixed mesh with $n_t = 12{,}354$ triangles, inner iterations of the Newton method are solved with varying N, with the upper triangular Gauss–Seidel preconditioner and LU factorization. They have confirmed the linear memory gain, independently of Re, with respect to the number of elements kept in the Fourier basis, as reported in Fig. 16 a). Analogously, the effect of mesh size on memory storage is also studied. The memory gain is reported in Fig. 16 b) as a function of the number of triangles. Curves correspond to different lengths of the truncated Fourier basis. Clearly, memory gain is independent of the mesh size, regardless of N.

3.3.3. Stability & sensitivity analysis

The stability of the steady state has been studied by Mizushima et al. [37]. They reported three types of instabilities, a symmetry breaking of the steady state via a pitchfork bifurcation, an oscillatory in-phase via a Hopf bifurcation, and a third oscillatory instability far from the near wake. For the chosen configuration ($g = 0.7$) the primary instability is a supercritical Hopf bifurcation at $Re \approx 57.5$ whose most unstable eigenmode is the in-phase oscillatory, *mode IP* partially reported in Fig. 17. The Floquet analysis reveals a pair of complex-conjugate multipliers on the in-phase synchronized vortex shedding periodic solution between the two cylinders. Neimark–Sacker appears at $Re_c = 61.7$, which is in good agreement with the result $Re_c = 61.8$ reported by Carini et al. [36].

Structural sensitivity, reported in Fig. 18, shows a symmetric averaged core of the instability in the near wake that is larger than the sensitive instability core of the single cylinder reported in Fig. 12. In addition, amplitudes of harmonic sensitivity are displayed in the frequency ω-axis. They provide further information about the origin of the flip-flop instability. Sensitive regions to harmonic structural perturbation are found for the first harmonic where it is possible to observe two sensitive regions around $y = \pm 2$ and a single one around $y = 0$ in the near wake for the second harmonic component. Remarkably, in this case, the instability is more sensitive to the second harmonic than the first one. The other sensitivity map, $\bar{\mathrm{S}}_\omega$ reported in Fig. 19, is particularly concentrated in the zone between cylinders. Not surprisingly, previous results in the literature indicate large variations of baseflow frequency as the gap ratio g is varied.

4. Conclusion

The computation of stability and sensitivity of periodic solutions provides access to inherent mechanisms leading to changes in dynamics. Efficient computational methods are essential for the computation of large-scale systems such as those arising from the semi-discretization of the governing equations. The spectral Fourier–Galerkin method is proposed for the efficient computation and continuation of autonomous problems. The methodology, though general, has been presented

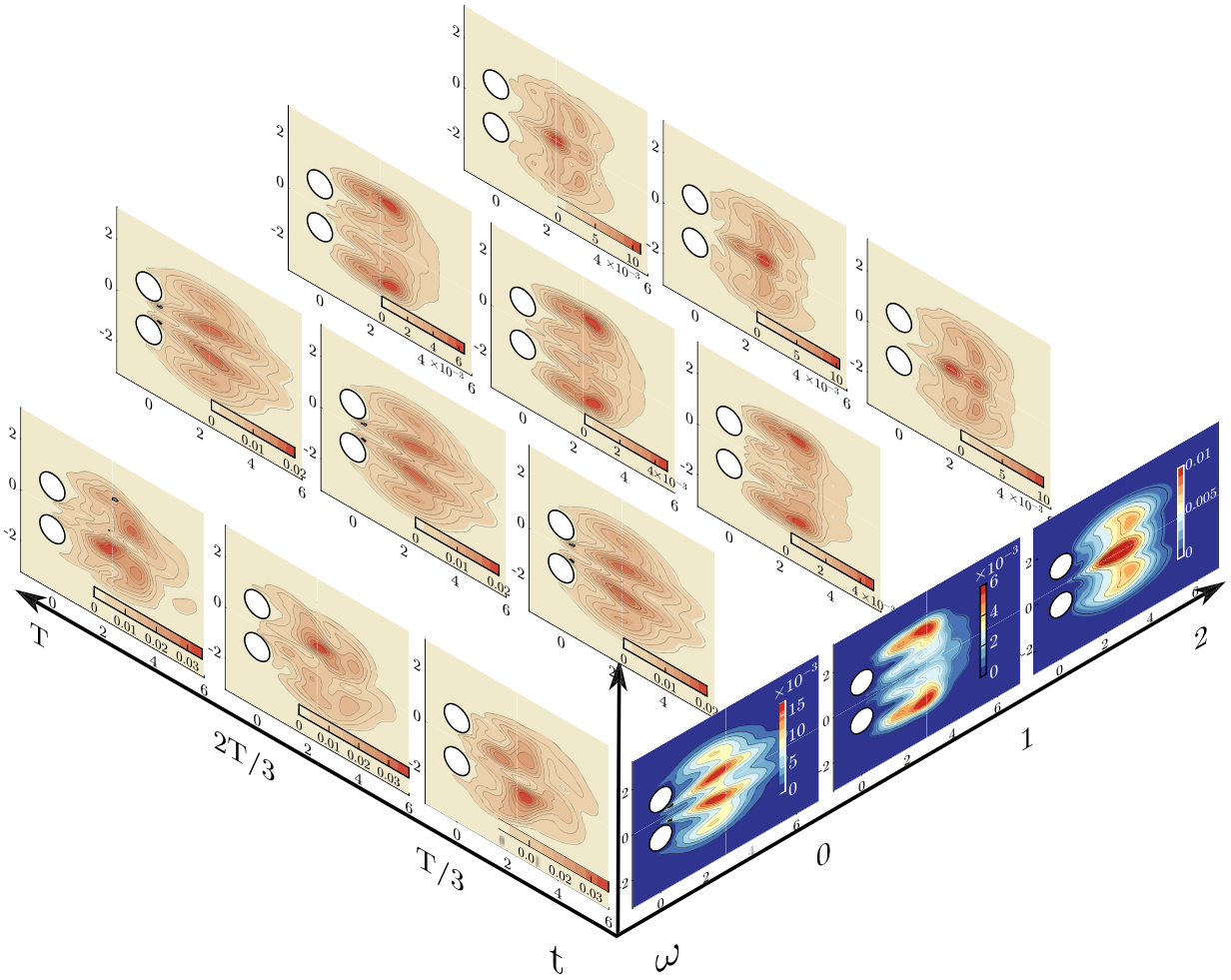

Fig. 18. Structural sensitivity $\mathrm{S}_s^{(\tau,N)}$ for $Re = 62$ with $N = 2$. t-axis: reconstruction of the spectral norm of the instantaneous structural sensitivity $\mathrm{S}_s^{(\tau,N)}(\mathbf{x}, t)$ at discrete instants $t = \{\frac{T}{3}, \frac{2T}{3}, T\}$. ω-axis: spectral norm of the modulus of harmonic sensitivity $|\mathrm{S}_s^{n;(\tau,N)}| = \sqrt{\mathrm{S}_s^{n,c;(\tau,N)^2} + \mathrm{S}_s^{n,s;(\tau,N)^2}}$ for harmonic components $n = \{0, 1, 2\}$. The spectral norm of the modulus of the harmonic sensitivity $|\mathrm{S}_s^{n;(\tau,N)}|$ is reconstructed in time at discrete instants.

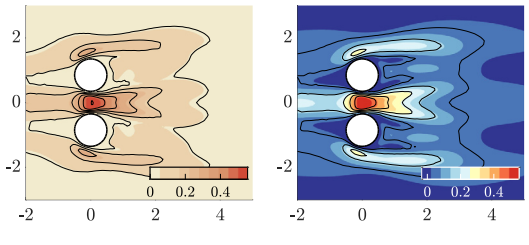

Fig. 19. Averaged sensitivity to frequency variations $\tilde{\mathrm{S}}_\omega^{(\tau,N)}$ of mode A at $Re = 190$, $k_z = 1.585$, and $N = 4$. a) Spectral norm. b) Trace.

for quadratic nonlinearities, where the frequency transform has a simple form, see appendix A.1. In the case of finite systems with few degrees of freedom, quadratic recasting is an option ([10,13]). However, such a recast increases the computational burden. It multiplies the number of degrees of freedom by a factor, which is not acceptable in large-scale systems. In those cases, an exact Fourier transform of nonlinear terms is required, see for instance the cubic nonlinearity of the compressible Navier–Stokes equations in Sierra et al. [38].

The present methodology is used to analyze three different scenarios. First, a toy model: Lorenz equations are used to display some of the properties of the methodology. Fourier–Galerkin strategy is employed for the continuation of unstable periodic orbits through a series of period-doubling bifurcations in the Feigenbaum route to chaos. Such a situation, usually studied by collocation or shooting methods, proves to be one of the worst-case scenarios for this kind of spectral method

due to the lack of smoothness of the system of equations, see Moore [39]. Regardless, the approach proves to be capable to compute partially and accurately this route to chaos at least in small systems, the continuation of the period-doubling cascade in large systems is still an open challenge for future studies.
Two fluid mechanics cases, archetypal of bluff body flows, are studied with the presented machinery. The vortex-shedding periodic flow past a circular cylinder and the flip-flop instability of two circular cylinders side-by-side have been accurately reconstructed with a finite number of harmonics. Such a set of examples have been employed to test the performance of the numerical resolution. The number of GMRES iterations is independent of the number of harmonics and it depends quadratically on the Reynolds number. Similarly, the memory gain of iterative methods with respect to a direct factorization increases linearly with the length of the truncated basis and it is independent of the mesh size. Two kinds of instabilities are analyzed, the transition of a two-dimensional periodic solution towards a three-dimensional periodic state and the flip-flop instability through a Neimark–Sacker bifurcation. Both instabilities mechanisms have been examined with the aid of sensitivity maps developed in section 2.5. Structural sensitivity of the periodic solution allows the identification of physical mechanisms causing self-sustained instabilities. Two types of instabilities have been reported in section 3: the spatio-temporal symmetry breaking in the case of two circular cylinders in tandem configuration, or the transition to a three-dimensional flow in the single circular cylinder configuration. In addition, sensitivity to frequency variations identifies those regions of the space where open-loop control will be most effective to cause a change in frequency. To conclude, the authors would like to remark that these sensitivity maps are easily computed under this framework, which is also more computationally efficient than direct time-integration in the studied configurations.

CRediT authorship contribution statement

The authors contributed equally to the submitted manuscript.

Declaration of competing interest

The authors declare that they have no known competing financial interests or personal relationships that could have appeared to influence the work reported in this paper.

Appendix A. Fourier–Galerkin equations

A.1. Nonlinear operator

Fourier–Galerkin equations (6) are derived by averaging truncated residual equations over a period T. Given the orthogonality of the Fourier basis, linear terms depend only on a harmonic whereas Fourier coefficients of the quadratic term $\mathbf{N}_i$ may depend on several of them. Here a detailed description of the quadratic terms is given:

$$
\begin{aligned}
\mathbf{N}_0 = {} & \mathbf{N}(\mathbf{q}_0,\mathbf{q}_0) + \tfrac{1}{2}\textstyle\sum_{i=1}^{N} \mathbf{N}(\mathbf{q}_{i,s},\mathbf{q}_{i,s}) + \mathbf{N}(\mathbf{q}_{i,c},\mathbf{q}_{i,c}) \\
\mathbf{N}_{i,c} = {} & \left[\mathbf{N}(\mathbf{q}_{i,c},\mathbf{q}_0) + \mathbf{N}(\mathbf{q}_0,\mathbf{q}_{i,c})\right] \\
& + \tfrac{1}{2}\textstyle\sum_{j=1}^{i-1} \left[\mathbf{N}(\mathbf{q}_{j,c},\mathbf{q}_{i-j,c}) - \mathbf{N}(\mathbf{q}_{j,s},\mathbf{q}_{i-j,s})\right] \\
& + \tfrac{1}{2}\textstyle\sum_{j=i+1}^{N} \left[\mathbf{N}(\mathbf{q}_{j,c},\mathbf{q}_{j-i,c}) + \mathbf{N}(\mathbf{q}_{j-i,s},\mathbf{q}_{j,s})\right] \\
& + \tfrac{1}{2}\textstyle\sum_{j=i+1}^{N} \left[\mathbf{N}(\mathbf{q}_{j-i,c},\mathbf{q}_{j,c}) + \mathbf{N}(\mathbf{q}_{j,s},\mathbf{q}_{j-i,s})\right] \\
\mathbf{N}_{i,s} = {} & \left[\mathbf{N}(\mathbf{q}_{i,s},\mathbf{q}_0) + \mathbf{N}(\mathbf{q}_0,\mathbf{q}_{i,s})\right] \\
& + \tfrac{1}{2}\textstyle\sum_{j=1}^{i-1} \left[\mathbf{N}(\mathbf{q}_{j,c},\mathbf{q}_{i-j,s}) + \mathbf{N}(\mathbf{q}_{j,s},\mathbf{q}_{i-j,c})\right] \\
& - \tfrac{1}{2}\textstyle\sum_{j=i+1}^{N} \left[\mathbf{N}(\mathbf{q}_{j,c},\mathbf{q}_{j-i,s}) + \mathbf{N}(\mathbf{q}_{j-i,s},\mathbf{q}_{j,c})\right] \\
& + \tfrac{1}{2}\textstyle\sum_{j=i+1}^{N} \left[\mathbf{N}(\mathbf{q}_{j-i,c},\mathbf{q}_{j,s}) + \mathbf{N}(\mathbf{q}_{j,s},\mathbf{q}_{j-i,c})\right].
\end{aligned}
$$

A.2. Residual notation

For the sake of a simpler presentation eq. (7) presents a series of operators, i.e., $\tilde{\mathbf{B}}, \tilde{\mathbf{L}}, \tilde{\mathbf{N}}$. Their definition is as follows:
Time derivative matrix $\tilde{\mathbf{B}}$

$$
\tilde{\mathbf{B}}\mathbf{Q}_N = \begin{bmatrix} \mathbf{0} & & & \\ & \mathbf{B}_1 & & \\ & & \ddots & \\ & & & \mathbf{B}_N \end{bmatrix} \begin{bmatrix} \mathbf{q}_0 \\ \mathbf{q}_1 \\ \vdots \\ \mathbf{q}_N \end{bmatrix} \text{ with } \mathbf{B}_n = \begin{bmatrix} \mathbf{0} & n\mathbf{B} \\ -n\mathbf{B} & \mathbf{0} \end{bmatrix} \text{ for } n = 1,\ldots,N. \tag{A.1}
$$

Linear operator $\tilde{\mathbf{L}}$

$$\tilde{\mathbf{L}}\mathbf{Q}_N = \begin{bmatrix} \mathbf{L} & & & \\ & \mathbf{L} & & \\ & & \ddots & \\ & & & \mathbf{L} \end{bmatrix} \begin{bmatrix} \mathbf{q}_0 \\ \mathbf{q}_1 \\ \vdots \\ \mathbf{q}_N \end{bmatrix} \text{ with } \mathbf{q}_n = \begin{bmatrix} \mathbf{q}_{n,c} \\ \mathbf{q}_{n,s} \end{bmatrix} \text{ for } n = 1, \dots, N. \tag{A.2}$$

Nonlinear operator $\tilde{\mathbf{N}}$

$$\tilde{\mathbf{N}}(\mathbf{Q}_N, \mathbf{Q}_N) = \begin{bmatrix} \mathbf{N}_0 \\ \mathbf{N}_1 \\ \vdots \\ \mathbf{N}_N \end{bmatrix} \text{ with } \mathbf{N}_n = \begin{bmatrix} \mathbf{N}_{n,c} \\ \mathbf{N}_{n,s} \end{bmatrix} \text{ for } n = 1, \dots, N. \tag{A.3}$$

A.3. Jacobian operator

Consider a small perturbation of $[\mathbf{Q}^{(\tau,N)}, \omega]^T$, here denoted as $[\delta\mathbf{Q}^{(\tau,N)}, \delta\omega]^T$, the linearized HBM equation is as follows:

$$\begin{aligned} \mathbf{0} &= -\delta\omega\tilde{\mathbf{B}}\mathbf{Q}_N - \omega\tilde{\mathbf{B}}\delta\mathbf{Q}^{(\tau,N)} + \tilde{\mathbf{L}}\delta\mathbf{Q}^{(\tau,N)} + D\tilde{\mathbf{N}}(\mathbf{Q}^{(\tau,N)})\delta\mathbf{Q}^{(\tau,N)} \\ &= -\delta\omega\tilde{\mathbf{B}}\mathbf{Q}^{(\tau,N)} + D\tilde{\mathbf{r}}(\mathbf{Q}^{(\tau,N)})\delta\mathbf{Q}^{(\tau,N)}, \end{aligned} \tag{A.4}$$

where the derivative of the quadratic operator is a dense block-symmetric matrix as follows:

$$D\tilde{\mathbf{N}}(\mathbf{Q}^{(\tau,N)}) = \begin{bmatrix} D\mathbf{N}^{(0)} & \dots & D\mathbf{N}^{(0,i)} & \dots & D\mathbf{N}^{(0,N)} \\ \vdots & \ddots & & & \vdots \\ D\mathbf{N}^{(i,0)} & \dots & D\mathbf{N}^{(i)} & \dots & D\mathbf{N}^{(i,N)} \\ \vdots & & & \ddots & \vdots \\ D\mathbf{N}^{(N,0)} & \dots & D\mathbf{N}^{(N,i)} & \dots & D\mathbf{N}^{(N)} \end{bmatrix}. \tag{A.5}$$

Let us consider the detailed description of each block. In the following, let us denote $D\mathbf{N}^{(\mathbf{q})} = \mathbf{N}(\cdot, \mathbf{q}) + \mathbf{N}(\mathbf{q}, \cdot)$, the linear operator of the derivative evaluated at $\mathbf{q}$.

Diagonal blocks $D\mathbf{N}^{(i)}$

$$D\mathbf{N}^{(0)} = D\mathbf{N}^{(\mathbf{q}_0)} \tag{A.6}$$

$$D\mathbf{N}^{(i)} = \begin{bmatrix} D\mathbf{N}^{(\mathbf{q}_0)} + \frac{1}{2}D\mathbf{N}^{(\mathbf{q}_{2i,c})} & \frac{1}{2}D\mathbf{N}^{(\mathbf{q}_{2i,s})} \\ \frac{1}{2}D\mathbf{N}^{(\mathbf{q}_{2i,s})} & D\mathbf{N}^{(\mathbf{q}_0)} - \frac{1}{2}D\mathbf{N}^{(\mathbf{q}_{2i,c})} \end{bmatrix} \text{ if } 0 < i \leq \frac{N}{2} \tag{A.7}$$

$$D\mathbf{N}^{(i)} = \begin{bmatrix} D\mathbf{N}^{(\mathbf{q}_0)} & \mathbf{0} \\ \mathbf{0} & D\mathbf{N}^{(\mathbf{q}_0)} \end{bmatrix} \text{ if } i > \frac{N}{2}. \tag{A.8}$$

Off diagonal-blocks $D\mathbf{N}^{(i,j)}$

$$D\mathbf{N}^{(0,j)} = \begin{bmatrix} \frac{1}{2}D\mathbf{N}^{(\mathbf{q}_{j,c})} & \frac{1}{2}D\mathbf{N}^{(\mathbf{q}_{j,s})} \end{bmatrix} \text{ if } j \neq 0, \tag{A.9}$$

$$D\mathbf{N}^{(i,0)} = \begin{bmatrix} \frac{1}{2}D\mathbf{N}^{(\mathbf{q}_{i,c})} \\ \frac{1}{2}D\mathbf{N}^{(\mathbf{q}_{i,s})} \end{bmatrix} \text{ if } i > 0. \tag{A.10}$$

If $i \neq j$, $j \neq 0$, $j < i$, $j + i \leq N$:

$$D\mathbf{N}^{(i,j)} = \begin{bmatrix} \frac{1}{2}D\mathbf{N}^{(\mathbf{q}_{i-j,c})} + \frac{1}{2}D\mathbf{N}^{(\mathbf{q}_{j+i,c})} & -\frac{1}{2}D\mathbf{N}^{(\mathbf{q}_{i-j,s})} - \frac{1}{2}D\mathbf{N}^{(\mathbf{q}_{j+i,s})} \\ \frac{1}{2}D\mathbf{N}^{(\mathbf{q}_{i-j,s})} + \frac{1}{2}D\mathbf{N}^{(\mathbf{q}_{j+i,s})} & \frac{1}{2}D\mathbf{N}^{(\mathbf{q}_{i-j,c})} + \frac{1}{2}D\mathbf{N}^{(\mathbf{q}_{j+i,c})} \end{bmatrix}. \tag{A.11}$$

If $i \neq j$, $j \neq 0$, $j < i$, $j + i > N$:

$$D\mathbf{N}^{(i,j)} = \begin{bmatrix} \frac{1}{2}D\mathbf{N}^{(\mathbf{q}_{i-j,c})} & -\frac{1}{2}D\mathbf{N}^{(\mathbf{q}_{i-j,s})} \\ \frac{1}{2}D\mathbf{N}^{(\mathbf{q}_{i-j,s})} & \frac{1}{2}D\mathbf{N}^{(\mathbf{q}_{i-j,c})} \end{bmatrix} \text{ if } i \neq j,\ j \neq 0,\ j < i, \tag{A.12}$$

otherwise $D\mathbf{N}^{(j,i)} = (D\mathbf{N}^{(i,j)})^T$.

Appendix B. Navier–Stokes operators

In the studied configurations, the flow is controlled by the Reynolds number $Re = \frac{U_\infty D}{\nu}$, U_∞ is the free stream velocity, D the diameter of the cylinder and ν the dynamic viscosity of the fluid. The fluid motion inside the domain is governed by the two-dimensional incompressible Navier–Stokes equations,

$$\frac{\partial \mathbf{U}}{\partial t} + \mathbf{U}\cdot\nabla\mathbf{U} = -\nabla P + \nabla\cdot\tau(\mathbf{U}) \tag{B.1a}$$

$$\nabla\cdot\mathbf{U} = 0, \tag{B.1b}$$

where $\mathbf{q} = [\mathbf{U}, P]$, $\mathbf{U}$ is the velocity vector whose components are (U, V), P is the reduced pressure and the viscous stress tensor $\tau(\mathbf{u})$ can be expressed as $\nu(\nabla\mathbf{U} + \nabla\mathbf{U}^T)$. The incompressible Navier–Stokes equations (B.1) are complemented with the following boundary conditions: on the cylinder surface, no-slip boundary conditions, uniform boundary conditions are set $U \to (U_\infty, 0)$ and stress-free at the outlet.

In the main text, Navier–Stokes equations (B.1) and the associated boundary conditions are written under the form $\mathbf{B}\frac{\partial \mathbf{q}}{\partial t} = \mathbf{L}\mathbf{q} + \mathbf{N}(\mathbf{q},\mathbf{q})$, where $\mathbf{N}(\mathbf{q},\mathbf{q}) = \mathbf{U}\cdot\nabla\mathbf{U}$ is the convective term.

References

[1] P. Cvitanović, Invariant measurement of strange sets in terms of cycles, Phys. Rev. Lett. 61 (24) (1988) 2729.
[2] G.M. Shroff, H.B. Keller, Stabilization of unstable procedures: the recursive projection method, SIAM J. Numer. Anal. 30 (4) (1993) 1099–1120.
[3] V. Citro, P. Luchini, F. Giannetti, F. Auteri, Efficient stabilization and acceleration of numerical simulation of fluid flows by residual recombination, J. Comput. Phys. 344 (2017) 234–246.
[4] E.J. Doedel, B. Oldeman, Auto-07p: Continuation and Bifurcation Software, 1998.
[5] A. Dhooge, W. Govaerts, Y.A. Kuznetsov, MATCONT: a MATLAB package for numerical bifurcation analysis of ODEs, ACM Trans. Math. Softw. 29 (2) (2003) 141–164.
[6] W. Govaerts, Y.A. Kuznetsov, V. De Witte, A. Dhooge, H. Meijer, W. Mestrom, A. Riet, B. Sautois, MATCONT and CL MATCONT: Continuation Toolboxes in Matlab, Gent University and Utrecht University, 2011.
[7] F. Giannetti, S. Camarri, V. Citro, Sensitivity analysis and passive control of the secondary instability in the wake of a cylinder, J. Fluid Mech. 864 (2019) 45–72.
[8] F. Giannetti, S. Camarri, P. Luchini, Structural sensitivity of the secondary instability in the wake of a circular cylinder, J. Fluid Mech. 651 (2010) 319–337.
[9] T. Kapitula, K. Promislow, Spectral and Dynamical Stability of Nonlinear Waves, vol. 185, Springer, 2013.
[10] L. Guillot, B. Cochelin, C. Vergez, A generic and efficient Taylor series-based continuation method using a quadratic recast of smooth nonlinear systems, Int. J. Numer. Methods Eng. 119 (4) (2019) 261–280.
[11] M. Urabe, Galerkin's procedure for nonlinear periodic systems, Arch. Ration. Mech. Anal. 20 (1965) 120–152.
[12] M. Krack, J. Gross, Harmonic Balance for Nonlinear Vibration Problems, Springer, 2019.
[13] B. Cochelin, C. Vergez, A high order purely frequency-based harmonic balance formulation for continuation of periodic solutions, J. Sound Vib. 324 (1–2) (2009) 243–262.
[14] A. Stokes, On the approximation of nonlinear oscillations, J. Differ. Equ. 12 (1972) 535–558.
[15] P. Kuchment, Floquet theory for hypoelliptic equations and systems in the whole space, in: Floquet Theory for Partial Differential Equations, Springer, 1993, pp. 103–123.
[16] Y.A. Kuznetsov, Elements of Applied Bifurcation Theory, vol. 112, Springer Science & Business Media, 2013.
[17] R. Seydel, Practical Bifurcation and Stability Analysis, vol. 5, Springer Science & Business Media, 2009.
[18] J. Zhou, T. Hagiwara, M. Araki, Spectral characteristics and eigenvalues computation of the harmonic state operators in continuous-time periodic systems, Syst. Control Lett. 53 (2) (2004) 141–155.
[19] C. Curtis, B. Deconinck, On the convergence of Hill's method, Math. Comput. 79 (269) (2010) 169–187.
[20] M.A. Johnson, K. Zumbrun, Convergence of Hill's method for non-self-adjoint operators, SIAM J. Numer. Anal. 50 (1) (2012) 64–78.
[21] B. Bentvelsen, A. Lazarus, Modal and stability analysis of structures in periodic elastic states: application to the Ziegler column, Nonlinear Dyn. 91 (2) (2018) 1349–1370.
[22] A. Lazarus, O. Thomas, A harmonic-based method for computing the stability of periodic solutions of dynamical systems, C. R., Méc. 338 (9) (2010) 510–517.
[23] L. Guillot, A. Lazarus, O. Thomas, C. Vergez, B. Cochelin, A purely frequency based Floquet–Hill formulation for the efficient stability computation of periodic solutions of ordinary differential systems, J. Comput. Phys. 416 (2020) 109477.
[24] F. Giannetti, P. Luchini, Structural sensitivity of the first instability of the cylinder wake, J. Fluid Mech. 581 (2007) 167–197.
[25] D. Sipp, Open-loop control of cavity oscillations with harmonic forcings, J. Fluid Mech. 708 (2012) 439.
[26] M. Benzi, M.A. Olshanskii, Z. Wang, Modified augmented Lagrangian preconditioners for the incompressible Navier–Stokes equations, Int. J. Numer. Methods Fluids 66 (4) (2011) 486–508.
[27] J. Moulin, P. Jolivet, O. Marquet, Augmented Lagrangian preconditioner for large-scale hydrodynamic stability analysis, Comput. Methods Appl. Mech. Eng. 351 (2019) 718–743.
[28] Y. Saad, Iterative Methods for Sparse Linear Systems, vol. 82, SIAM, 2003.
[29] F. Hecht, New development in FreeFem++, J. Numer. Math. 20 (3–4) (2012) 251–266.
[30] S. Balay, S. Abhyankar, M. Adams, J. Brown, P. Brune, K. Buschelman, L. Dalcin, A. Dener, V. Eijkhout, W. Gropp, et al., PETSc Users Manual, 2019.
[31] V. Hernandez, J.E. Roman, V. Vidal, SLEPc: a scalable and flexible toolkit for the solution of eigenvalue problems, ACM Trans. Math. Softw. 31 (3) (2005) 351–362.
[32] D. Fabre, V. Citro, D. Ferreira Sabino, P. Bonnefis, J. Sierra, F. Giannetti, M. Pigou, A practical review on linear and nonlinear global approaches to flow instabilities, Appl. Mech. Rev. 70 (6) (2018).
[33] P. Collet, J.-P. Eckmann, O. Lanford, Universal properties of maps on an interval, Commun. Math. Phys. 76 (3) (1980) 211–254.
[34] C.H.K. Williamson, Vortex dynamics in the cylinder wake, Annu. Rev. Fluid Mech. 28 (1) (1996) 477–539.
[35] D. Barkley, R.D. Henderson, Three-dimensional Floquet stability analysis of the wake of a circular cylinder, J. Fluid Mech. 322 (1996) 215–241.
[36] M. Carini, F. Giannetti, F. Auteri, On the origin of the flip-flop instability of two side-by-side cylinder wakes, J. Fluid Mech. 742 (2014) 552–576.

[37] J. Mizushima, Y. Ino, Stability of flows past a pair of circular cylinders in a side-by-side arrangement, J. Fluid Mech. 595 (2008) 491–507.
[38] J. Sierra, V. Citro, F. Giannetti, D. Fabre, Efficient computation of periodic compressible flows with spectral techniques, 2020, Manuscript submitted for publication.
[39] G. Moore, Floquet theory as a computational tool, SIAM J. Numer. Anal. 42 (6) (2005) 2522–2568.